



Upconversion luminescence properties and thermal quenching mechanisms in the layered perovskite $\text{La}_{1.9}\text{Er}_{0.1}\text{Ti}_2\text{O}_7$ towards an application as optical temperature sensor

Alexandre Bayart, Fabien Szczepanski, Jean-François Blach, Jolanta Rousseau, Arturas Katelnikovas, Sébastien Saitzek

► To cite this version:

Alexandre Bayart, Fabien Szczepanski, Jean-François Blach, Jolanta Rousseau, Arturas Katelnikovas, et al.. Upconversion luminescence properties and thermal quenching mechanisms in the layered perovskite $\text{La}_{1.9}\text{Er}_{0.1}\text{Ti}_2\text{O}_7$ towards an application as optical temperature sensor. *Journal of Alloys and Compounds*, 2018, 744, pp.516 - 527. 10.1016/j.jallcom.2018.02.055 . hal-01716248

HAL Id: hal-01716248

<https://hal.science/hal-01716248v1>

Submitted on 20 Nov 2023

HAL is a multi-disciplinary open access archive for the deposit and dissemination of scientific research documents, whether they are published or not. The documents may come from teaching and research institutions in France or abroad, or from public or private research centers.

L'archive ouverte pluridisciplinaire **HAL**, est destinée au dépôt et à la diffusion de documents scientifiques de niveau recherche, publiés ou non, émanant des établissements d'enseignement et de recherche français ou étrangers, des laboratoires publics ou privés.



Distributed under a Creative Commons Attribution - NonCommercial - NoDerivatives 4.0 International License

Upconversion luminescence properties and thermal quenching mechanisms in the layered perovskite $\text{La}_{1.9}\text{Er}_{0.1}\text{Ti}_2\text{O}_7$ towards an application as optical temperature sensor

Alexandre Bayart¹, Fabien Szczepanski¹, Jean François Blach¹, Jolanta Rousseau¹, Arturas Katelnikovas², Sébastien Saitzek^{1,*}

¹ Univ. Artois, CNRS, Centrale Lille, ENSCL, Univ. Lille, UMR 8181, Unité de Catalyse et Chimie du Solide (UCCS), F-62300 Lens, France

² Vilnius University, Faculty of Chemistry and Geosciences, Institute of Chemistry, Naugarduko 24, Vilnius, LT-03225, Lithuania

***Corresponding author:**

Sébastien SAITZEK,

¹Université d'Artois, Unité de Catalyse et de Chimie du Solide, UCCS,
Axe Chimie du Solide, CNRS-UMR 8181, Faculté des Sciences Jean Perrin,
F-62300 LENS, France

Phone: +33 / 321791732, Fax: +33 / 321177955, E-mail: sebastien.saitzek@univ-artois.fr

Abstract

The structural evolution between the monoclinic (layered-perovskite) and cubic (pyrochlore) structures is studied for the complete series of $\text{La}_{2-x}\text{Er}_x\text{Ti}_2\text{O}_7$ synthesized by solid-state reaction. A partial solid solution with layered perovskite structure is achieved until $x = 0.10$. The luminescence properties of these oxides show a low quantum efficiency and the concentration quenching is observed for $x = 0.10$. However, $\text{La}_{1.9}\text{Er}_{0.1}\text{Ti}_2\text{O}_7$ oxide exhibits interesting upconversion (UC) properties at multiple excitation wavelengths (784, 808 and 980 nm). Laser power studies have demonstrated a two-photon upconversion process for 808 and 980 nm excitations. Moreover, the measurement of the lifetimes on the $^4\text{F}_{9/2} \rightarrow ^4\text{I}_{15/2}$ and $^4\text{S}_{3/2} \rightarrow ^4\text{I}_{15/2}$ transitions makes it possible to identify an Energy Transfer (ET) mechanism. The thermal effect on upconversion properties is also studied under 808 nm excitation. The UC intensity shows atypical evolutions: $^4\text{F}_{9/2} \rightarrow ^4\text{I}_{15/2}$ transition follows a continuous decrease as a function of temperature, while $^4\text{S}_{3/2} \rightarrow ^4\text{I}_{15/2}$ and $^2\text{H}_{11/2} \rightarrow ^4\text{I}_{15/2}$ transitions reach maxima at 150 and 450 K, respectively. The calculation of temperature dependent Fluorescence Intensity Ratio and CIE 1931 color coordinates indicated that $\text{La}_{1.9}\text{Er}_{0.1}\text{Ti}_2\text{O}_7$ oxide could serve as a temperature sensor.

Keywords: Layered-Perovskite, X-Ray Diffraction, Luminescence Properties, Upconversion Properties, Thermal Quenching

1.Introduction

The absorption of two or more photons leading to the emission of light at a wavelength shorter than the excitation wavelength is described as the upconversion (UC) process. It is a nonlinear optical process also named anti-Stokes emission. Historically, the theoretical absorption process involving two photons was initially described by N. Bloembergen in 1959

[1] giving it the name of "quantum counter action". But, the first experimental observations were performed in 1966 by F. Auzel [2] on tungstates and independently by V. V. Ovsyankin and P. P. Feofilov on Erbium-doped BaF₂ crystals [3]. Since then, upconversion luminescence materials are gaining increasing interest of the scientific community due to their strong application potential. Firstly, UC materials are used in many optical devices such as solid-state lasers [4], temperature sensors [5], optical fibers [6], NIR quantum counter detectors [7] or the displays technologies [8]. Secondly, these materials can also be employed to improve the performance of photovoltaics devices. Indeed, using an upconversion layer between the photovoltaic material and the back reflector allows to harvest a wider range of solar energy by converting NIR to visible (or UV) radiations. The UC layer absorbs two (or more) photons and then re-emits a photon at a shorter wavelength corresponding to the best response of the Photovoltaic (PV) device. This process is not to be confused with the down-shifting effect where one photon of high energy, which is inefficiently absorbed by the photovoltaic material is converted to one photon of low energy that can be more efficiently absorbed by the photovoltaic material [9]. Finally, UC nanoparticles are widely used in biological applications where the active nanoparticles are generally encapsulated for biocompatibilities reasons and functionalized for the specific targeting. These UC nanoparticles can be employed for biological labeling [10], *in vivo* bio-imaging by UC microscopy [11], highly sensitive bioassays [12], the photodynamic therapy [13] or the photoactivated drug delivery system [9] (NIR to visible upconversion materials are interesting because their excitation wavelength locates within the NIR optical window of biological tissues; it can thus reach the maximum penetration).

Among the materials with upconversion properties those with Er³⁺ ions (such as NaYF₄:Er³⁺ [14], Y₂O₃:Er³⁺ [15], etc.) are the most studied [16]. In this study, the multifunctional La₂Ti₂O₇ oxide will be used as a host matrix to develop phosphors with upconversion properties. This oxide is already known for its ferroelectric [17],[18] and piezoelectric [19] properties with high

Curie temperature ($T_C \sim 1461 \pm 5^\circ\text{C}$) enabling use in severe environments such as those encountered in the aeronautics or space [20]. Apart from these applications, this compound also possesses good photocatalytic properties, in particular for the H_2 production by the water-splitting [21] or for the Volatile Organic Compounds (VOCs) degradation [22]. Moreover, for the close ionic radii, it can serve as a host matrix in order to develop phosphors by the substitution of the La site with other lanthanides. Several studies have been carried out on these oxides with substitutions of Ln by Pr^{3+} , Sm^{3+} or Eu^{3+} , Er^{3+} and Tb^{3+} [23], [24], [25], [26]. On the same principle, the ionic radii of lanthanides and actinides are also fairly close. It is also possible to substitute site A with radionuclides. Moreover, their good resistance to amorphization under ionizing radiation makes it possible to realize immobilization matrix for nuclear wastes [17],[27],[28].

$\text{La}_2\text{Ti}_2\text{O}_7$ oxide belong to the $\text{A}_n\text{B}_n\text{O}_{3n+2}$ family [29] with $n = 4$ (i.e. $\text{La}_4\text{Ti}_4\text{O}_{14}$ or more generally called $\text{La}_2\text{Ti}_2\text{O}_7$). $\text{La}_2\text{Ti}_2\text{O}_7$ have a monoclinic crystal system and lattice parameters are: $a = 7.800(3) \text{ \AA}$, $b = 5.546(2) \text{ \AA}$, $c = 13.011(4) \text{ \AA}$ and $\beta = 98.60(2)^\circ$ [30]. Above 780°C , this symmetry becomes orthorhombic with $\text{Cmc}2_1$ space group [31]. The unit cell is described by four layers ($n = 4$) of corner-sharing TiO_6 octahedra separated by two layers of La-site cations [17]. There are two possibilities for positioning the Ln^{3+} cations in this structure [17]. The first ones are located between the perovskite cage defined by TiO_6 octahedra and the second ones are positioned between the slabs of octahedra. More generally, $\text{Ln}_2\text{Ti}_2\text{O}_7$ compounds present two structures according to the ratio between the radii of Ln^{3+} and Ti^{4+} cations. For $r(\text{Ln}^{3+})/r(\text{Ti}^{4+}) = 1.46$ to 1.78 i.e. $\text{Ln} = \text{Sm}$ to Lu , the cubic/pyrochlore structure with $Fd\bar{3}m$ space group is privileged. For $r(\text{Ln}^{3+})/r(\text{Ti}^{4+}) > 1.78$ (i.e. $\text{Ln} = \text{La}$ to Nd), the monoclinic/layered-perovskite structure with $P2_1$ space group is favored [17]. Since their discovery, many studies have been performed on the synthesis of $\text{Ln}_2\text{Ti}_2\text{O}_7$ oxides by solid state reaction [32], [33], spray pyrolysis [34], polymeric complex method [21], sol-gel route [35],[24], hydrothermal

synthesis [36], metal-organic decomposition methods [37], urea precipitation [38] or the floating zone method for single crystals [39].

The upconversion properties within $\text{La}_2\text{Ti}_2\text{O}_7\text{:Er}^{3+}$ oxides elaborated by sol-gel for an excitation of 980 nm were highlighted by X. Li *et al.* [26]. To complete their studies, we propose to study $\text{La}_{2-x}\text{Er}_x\text{Ti}_2\text{O}_7$ oxides synthesized by solid state reaction. In this present work, we will study: i) the classical luminescence properties and the quantum efficiency; ii) the upconversion effects under other Visible or NIR sources (784, 808 and 980 nm) and their multiple photon absorption mechanisms; iii) the lifetime of the upconversion process; iv) the Thermal Quenching (TQ) mechanisms; and v) the colorimetric properties.

Finally, this oxide exhibits suitable properties for an optical temperature sensor application with good thermal sensitivity. A sensor based on the temperature-dependent Fluorescence Intensity Ratio (FIR) will be discussed.

2. Experimental section

A conventional solid state reaction was used to synthesize the $\text{La}_{2-x}\text{Er}_x\text{Ti}_2\text{O}_7$ powders. The starting materials are lanthanide oxides such as La_2O_3 and Er_2O_3 (99.99% Strem Chemicals) and titanium dioxide TiO_2 (99.99% Sigma-Aldrich). These precursor oxides were weighed in stoichiometric proportions and ground for 20 min with ethanol. The mixture was then calcined in an alumina crucible at 1100 °C for 12 h. The calcination and milling steps were repeated twice to improve the sample homogeneity. Lanthanum oxide is hygroscopic. In this respect, they require a thermal pre-treatment before weighing in order to avoid the formation of hydroxide which will disrupt the final stoichiometry.

Thermal Analyses have been performed using a TGA/DSC 3+ STARe System (Mettler Toledo). The scan rate is 5 °C/min under an air flow of 40 mL/min.

A Perkin Elmer Lambda 19 ultraviolet-visible spectrometer was used to characterize the optical properties of $\text{La}_{1.9}\text{Er}_{0.1}\text{Ti}_2\text{O}_7$ oxides. The diffuse reflection spectra were carried out between 220 and 800 nm and Tauc plot [40] was used to determine the optical band gap.

For structural characterizations, a Rigaku Ultima IV X-Ray diffractometer equipped with Cu anticathode ($\lambda K_\alpha = 1.5418 \text{ \AA}$) was employed. Soller slits to limit the divergence of X-ray beam and a nickel foil filter to attenuate Cu K_β were used. All XRD patterns were recorded in the range of 10° - 90° , with a step of 0.02° and with a speed of $0.1^\circ/\text{min}$.

Room-temperature excitation and emission spectra were recorded on the Edinburgh Instruments FLS980 spectrometer equipped with a double excitation and emission monochromators, in the range of 250-900 nm. The excitation spectra were corrected by a reference detector and emission spectra by correction file obtained from a tungsten incandescent lamp certified by NPL (National Physics Laboratory, UK). For upconversion measurements, two CW (Continuous Wave) lasers emitting at 808 and 980 nm were used in order to excite the sample. An ultra-fast detector was employed for kinetic measurements and the integration sphere was used for the Quantum Efficiency (QE) measurements. For Thermal Quenching (TQ) measurements, a cryostat “MicrostatN” from the Oxford Instruments had been coupled to the Edinburgh Instruments FLS980 spectrometer. Liquid nitrogen was used as a cooling agent. The measurements were performed at 77 K and at 100–500 K with 50 K steps. Temperature stabilization time was 90 s and temperature tolerance was set to $\pm 5 \text{ K}$. During the measurements, dried nitrogen was flushed over the cryostat window to avoid the condensation of water at low temperatures on the window surface. Finally, the chromaticity coordinates (Commission Internationale de l’Éclairage – CIE 1931) were calculated from the emission spectra. The color coordinates were calculated in the range 360-830 nm. The whole emission spectrum was taken into account.

3. Results and Discussions

3.1 Structural Characterizations

The solid state reaction was used to prepare the series of oxides. In order to determine the experimental conditions for obtaining the $\text{La}_2\text{Ti}_2\text{O}_7$ oxides, a ThermoGravimetric Analysis (TGA) coupled to a Differential Thermal Analysis (DTA) was carried out on the starting precursors (Figure 1). Follow-up with loss of mass shows four successive jumps. The first one, located at relatively low temperatures (40-150 °C), is due to the evaporation of the adsorbed water on the starting materials. The second and third jumps (between 300/450 °C and 450/600 °C, respectively) show significant mass losses corresponding to 6.30% and 2.89%, respectively. These are also accompanied by endothermic reactions at 385 and 525 °C evoking the dehydration of $\text{La}(\text{OH})_3$. Indeed, it has been reported that the dehydration of the lanthanum hydroxide is generally carried out in two steps by the following reactions [41]: $2\text{La}(\text{OH})_3 \rightarrow 2\text{LaOOH} + 2\text{H}_2\text{O}$ and $2\text{LaOOH} \rightarrow \text{La}_2\text{O}_3 + \text{H}_2\text{O}$.

The last jump associated with a mass loss is between 600 and 1100 °C. This one cannot be attributed to a reaction between the starting precursors because the reaction ($\text{La}_2\text{O}_3 + 2\text{TiO}_2 \rightarrow \text{La}_2\text{Ti}_2\text{O}_7$) is not accompanied by a loss of mass. In fact, this loss is due to the presence of carbon dioxide in the atmosphere which can cause carbonation of part of the lanthanum oxide ($\text{La}_2\text{O}_3 + \text{CO}_2 \rightarrow \text{La}_2\text{O}_2\text{CO}_3$) and then its decarbonation at higher temperature with slow kinetics. This phenomenon is described in the works of B. Backiz et al. [42] on kinetic phenomena related to decarbonation and in the works of E. Füglein et al. [43] showing the release of CO_2 by TGA measurements coupled to IR spectrometer. Therefore, the fourth jump can be attributed to the decarbonation phenomenon. This result also indicates that the Ln_2O_3 starting precursors must undergo a pretreatment at least up to 800 °C before the weighing because these are highly hygroscopic. Moreover, the maximum mass loss is reached around 1100 °C. This temperature has therefore been chosen for the synthesis of the $\text{La}_2\text{Ti}_2\text{O}_7$ oxides.

The structural characterization on the $\text{La}_{2-x}\text{Er}_x\text{Ti}_2\text{O}_7$ series was performed employing powder X-ray diffraction. Figure 2.a presents the XRD patterns obtained for $\text{La}_{2-x}\text{Er}_x\text{Ti}_2\text{O}_7$ with $x = 0-2$. Initially, for $x = 0$, a $\text{La}_2\text{Ti}_2\text{O}_7$ single-phase (JCPDS No 81-1066) was obtained with the layered-perovskite/monoclinic structure. Using a profile matching method for the refinement, the lattice parameters are: $a = 7.809(2) \text{ \AA}$, $b = 5.546(7) \text{ \AA}$, $c = 13.008(1) \text{ \AA}$ and $\beta = 98.629(5)^\circ$. Then, for low substitution rates until $x = 0.10$, only a layered perovskite phase is synthesized without additional peaks (Figure 2.b). While for higher substitution rates, a mixture of two phases (constituted of a substituted monoclinic phase and the $\text{Er}_2\text{Ti}_2\text{O}_7$ oxide in the cubic structure) is obtained. Finally, for $x = 2$, we synthesize a unique $\text{Er}_2\text{Ti}_2\text{O}_7$ phase (JCPDS No. 18-0499) which crystallizes with a cubic/pyrochlore structure ($Fd\bar{3}m$). The refined cell parameter is $a = 10.074(3) \text{ \AA}$.

Furthermore, for low substitution rates, XRD patterns of $\text{La}_{1-x}\text{Er}_x\text{Ti}_2\text{O}_7$ show a small shift towards the large angles for the (hkl) reflections according to the x value. This shift is more marked when h and $k \neq 0$, while $(00l)$ reflections are not modified. This behaviour can be noticed by zooming into the XRD patterns in the range $2\theta = 27.5^\circ$ to 28.5° (Figure 2.c). This displacement towards the wide angle reflects a decrease of the unit cell. More specifically, the a and b cell parameters decrease with x increase. While the c cell parameter remains substantially constant, regardless the x value. For substitution with a lanthanide of smaller ionic radius, similar results have been observed in previous study [25]. In this case, this behavior is not surprising. Indeed, the variation of the cationic size ($v_{\text{III}}\text{La}^{3+} = 1.160 \text{ \AA}$ to $v_{\text{III}}\text{Er}^{3+} = 1.004 \text{ \AA}$) inside the perovskite cage has a great influence on TiO_6 octahedra chains which are infinite along the \vec{a} - and \vec{b} -axes. Separately, along the c -axis, Ln-interleaves (interlayer between sheets) are placed in a less dense layer which can be modified to counterbalance the cationic modification and permits to explain the relative stability of the c cell parameter. Indeed, Zhang

et al. [44] have shown that the greatest compressibility can be realized along \vec{c} -axis. This explains also the persistence of the cell parameter in this direction.

3.2 Luminescence properties

For one composition $x = 0.2$, the luminescence properties (excitation and emission spectra) have already been studied in our previous work [25]. In this part, we propose to extend this work in order to identify the quenching concentration and the most efficient sample. In order to assess the influence of the substitution rate on the intensity of luminescent in the $(\text{La}_{1-x}\text{Er}_x)_2\text{Ti}_2\text{O}_7$ oxides, the emission spectra according to x values have been measured under 377 nm excitation. All of them are of similar shape and the typical room-temperature excitation and emission spectra of $\text{La}_{1.90}\text{Er}_{0.10}\text{Ti}_2\text{O}_7$ are presented on Figure 3a. Firstly, the excitation spectrum (black line) possesses a broad band in the range of 250 – 325 nm due to the host-matrix absorption (this value is correlated with the optical band gap determined in Figure S1-Supplementary Information). Moreover, several peaks corresponding to the intraconfigurational $[\text{Xe}]4f^{11} - [\text{Xe}]4f^{11}$ transitions [45] of Er^{3+} ($^4\text{I}_{15/2} \rightarrow ^2\text{K}_{15/2}$; $^4\text{G}_{9/2}$ (350 – 370 nm), $^4\text{I}_{15/2} \rightarrow ^4\text{G}_{11/2}$ (377 nm), $^4\text{I}_{15/2} \rightarrow ^2\text{H}_{9/2}$ (406 nm), $^4\text{I}_{15/2} \rightarrow ^4\text{F}_{3/2}$; $^4\text{F}_{5/2}$ (452 nm) transitions [46]) are also observed. For the emission spectrum (red line), many intense peaks centered in the green spectral domain ($\lambda = 520$ nm to 570 nm) are highlighted. These peaks can be attributed to the $^2\text{H}_{11/2} \rightarrow ^4\text{I}_{15/2}$ and $^4\text{S}_{3/2} \rightarrow ^4\text{I}_{15/2}$ transitions [47], respectively (Figure 3b). In addition, some less intense bands centered between 660 and 680 nm may be indexed with the $^4\text{F}_{9/2} \rightarrow ^4\text{I}_{15/2}$ transition. We noticed a multitude of peaks which can be attributed to a modification of electronic states by a Stark effect [48].

The CIE Chromaticity coordinates of $\text{La}_{1.90}\text{Er}_{0.10}\text{Ti}_2\text{O}_7$ are calculated to be ($x = 0.2812$; $y = 0.7008$) and the luminous efficacy is 607 lm/W_{opt} (Figure 3c). The Quantum Efficiency

(QE) was determined using an integration sphere and was measured to be 3.63% for an excitation wavelength of 377 nm. This value is rather low compared to substitutions such as Eu^{3+} where it can reach 42% [25].

Using integrated emission values, a concentration quenching effect is highlighted around $x = 0.10$ (Figure 3.d). This behaviour is due to the ET between Er^{3+} activator ions. The knowledge of the critical distance (R_c) is important to obtain information about interaction mechanism. The value of R_c can be calculated from the following equation [49]:

$$R_c = 2 \left(\frac{3V}{4\pi x_c N} \right)^{1/3} \quad (1)$$

Where V is the volume of the unit cell, x_c is the activator concentration where the quenching occurs and N is the number of ions whose sites are partially occupied by the activator in the unit cell (in our case $N = 4$). In this work and for $x_c = 0.10$, the critical transfer distance of the exchange interaction is about 13.8 Å. To the best of our knowledge, the typical critical distance is around 5 Å [50]. However, the calculated R_c value is greater. This tells us that electric multipolar interactions are significant in these phosphors.

The room temperature photoluminescence decay curve of $^4\text{S}_{3/2} \rightarrow ^4\text{I}_{15/2}$ transition in $\text{La}_{1.90}\text{Er}_{0.10}\text{Ti}_2\text{O}_7$ oxide is presented in the Figure 3e. This decay curve can be fitted successfully with a classical double exponential equation [51]:

$$I(t) = I_0 + A_1 e^{\left(\frac{-t}{\tau_1}\right)} + A_2 e^{\left(\frac{-t}{\tau_2}\right)} \quad (2)$$

Where, $I(t)$ is the luminescence intensity at time t and I_0 is the initial intensity. A_1 and A_2 are constants related to the initial intensity, τ_1 and τ_2 are the lifetimes of the each exponential component. The average lifetime constant $\bar{\tau}$ can be also calculated by the following equation [52], [53]:

$$\bar{\tau} = \frac{\sum_i A_i \tau_i^2}{\sum_i A_i \tau_i} \quad (3)$$

The measured average fluorescence lifetimes ($\bar{\tau}$) were calculated to be 32.9 μ s. The double exponential model demonstrates multiple environment for Er^{3+} cations. This can be elucidated by the presence of two crystallographic sites in the monoclinic structure. The substitution can be performed randomly on a Ln^{3+} sites situated in the sheets or in the interlayers.

3.3 Upconversion properties

Upconversion luminescence properties of $\text{La}_{2-x}\text{Er}_x\text{Ti}_2\text{O}_7$ powder were checked using two lasers emitting at 808 and 980 nm. We have adjusted the laser power to reveal the evolution of luminescence intensity with the power of the excitation line. The results are summarized in Figure 4.

The $\text{La}_{2-x}\text{Er}_x\text{Ti}_2\text{O}_7$ powder emits a strong green light, which corresponds to the intense peaks situated in the 514-575 nm range, and a weak red light, which corresponds to the peaks situated in the 640-690 nm range, when excited by near infrared lasers with wavelengths of 808 or 980 nm. These peaks can be easily attributed to transitions of Er^{3+} : the intense green peaks centered at 525 and 548 nm correspond to $^2\text{H}_{11/2} \rightarrow ^4\text{I}_{15/2}$ and $^4\text{S}_{3/2} \rightarrow ^4\text{I}_{15/2}$ transitions of Er^{3+} ion, respectively; the red peaks centered at 660 nm correspond to the $^4\text{F}_{9/2} \rightarrow ^4\text{I}_{15/2}$ transition of Er^{3+} ion. As the conventional luminescence, the multitude of peaks observed is certainly due to a modification of the electronic states by the Stark effect [48].

The mechanism of absorption in upconversion luminescence is more complicated than conventional fluorescence and can be described by the three main mechanisms[1]-[3]: Excited-State Absorption (ESA), Energy Transfer (ET), and Photon Avalanche (PA). The usual method to find the mechanism consists of plotting $\text{Ln}(I)$ versus $\text{Ln}(P)$, where I and P are the integrated intensity of luminescence and the laser power, respectively. The slope of this curve indicates the number of photons involved in the absorption process. A bending point can indicate the

presence of photon avalanche process. In our case, this bending point is not observed and therefore the photon avalanche process can be excluded.

The slope of the curves $\ln(I)$ versus $\ln(P)$ (Figure 5) was 1.84, 1.78, 1.46 for the population of $^2H_{11/2}$, $^4S_{3/2}$, $^4F_{9/2}$ levels under 808 nm excitation and 1.44, 1.36, 1.32 for the population of $^2H_{11/2}$, $^4S_{3/2}$, $^4F_{9/2}$ levels under 980 nm excitation, respectively. We can suggest that two photons are required to create these mechanisms. It is worth noting that there is a saturation effect (Figure 5a) in the case of the excitation with the 808 nm laser at high power. This saturation is not visible with the 980 nm laser because its maximum power is limited to 1 W (Figure 5b). This saturation is usually explained by a long life time of excited states [54] or by a competition between the UC mechanisms and the depletion of intermediate states under continuous laser excitation [54]. With the hypothesis of absorption of two photons for the upconversion, we propose the mechanisms described in Figure 6. We propose the following model for the wavelength of 980 nm: one photon is absorbed from $^4I_{15/2}$ to $^4I_{11/2}$ (Ground State Absorption – GSA); another photon (ESA) is then absorbed from this state to $^4F_{7/2}$ state. A relaxation process involving phonons can populate $^4S_{3/2}$ and $^4F_{9/2}$; these levels are responsible to light emission at 548 and 660 nm observed experimentally, respectively (it will be shown latter, the $^2H_{11/2}$ level, responsible for emission at ca. 525 nm, is thermally populated from $^4S_{3/2}$ level). We cannot exclude a second route for upconversion based on ET process. In this case, one ion is excited from $^4I_{15/2}$ to $^4I_{11/2}$, its energy is then transferred to a neighbouring ion in the same state $^4I_{11/2}$, and the latter is promoted to the $^4F_{7/2}$ state. The phonon relaxation phenomena explained the green and red emission. Regarding the absorption of 808 nm laser, we propose the following model: Er^{3+} ion is promoted from the ground state $^4I_{15/2}$ to the excited state $^4I_{9/2}$. Quickly, there is a non-radiative relaxation to the metastable state $^4I_{13/2}$ [55]. The life time of this level is long enough for the second absorption (ESA) of 808 nm photon. This absorption populates the $^4S_{3/2}$ level, which in turn populates $^2H_{11/2}$ and $^4F_{9/2}$ states. The three later states can explain the

presence of green and red lines in the emission spectra. As for the 980 nm laser, we can also include in our model the presence of energy transfer process from a neighbouring ion excited at $^4I_{9/2}$ state to a second ion in the same state. The conclusions are the same as for the ESA process.

It is also interesting to note that the relative intensity of emission originating from the ($^2H_{11/2} + ^4S_{3/2}$) \rightarrow $^4I_{15/2}$ and $^4F_{9/2} \rightarrow ^4I_{15/2}$ transitions changes with the laser wavelength (see Figure 4). Excitation with 980 nm laser yields stronger intensity of $^4F_{9/2} \rightarrow ^4I_{15/2}$ transition in the red spectral region if compared to the excitation with 808 nm laser. There is one common $^4F_{9/2}$ level population pathway regarding both excitation wavelengths, i.e. multiphonon relaxation from $^2H_{11/2}$ and $^4S_{3/2}$ levels. However, under 980 nm excitation, Er^{3+} ions from the excited $^4I_{11/2}$ level can relax to the lower lying $^4I_{13/2}$ level, which, in turn, is excited by another photon to the $^4F_{9/2}$ level (see Figure 6), thus opening another channel for $^4F_{9/2}$ population leading to stronger emission in red.

The time-resolved measurements performed on $^4S_{3/2} \rightarrow ^4I_{15/2}$ and $^4F_{9/2} \rightarrow ^4I_{15/2}$ transitions at 980 nm are shown in Figure 7, and this reveal an energy transfer between Er^{3+} ions [56]. Indeed, the fast initial increase in the upconversion intensity observed before the decays is a distinctive characteristic of this process. The curves were fitted with a usual exponential decay curve [57] and precisely with a sum of exponential decays curves: three exponential decays curves for the $^4S_{3/2} \rightarrow ^4I_{15/2}$ transition $I(t) = I_0 + A_1 e^{\left(\frac{-t}{\tau_1}\right)} + A_2 e^{\left(\frac{-t}{\tau_2}\right)} + A_3 e^{\left(\frac{-t}{\tau_3}\right)}$ and two exponential decays curves for the $^4F_{9/2} \rightarrow ^4I_{15/2}$ transition $I(t) = I_0 + A_1 e^{\left(\frac{-t}{\tau_1}\right)} + A_2 e^{\left(\frac{-t}{\tau_2}\right)}$. Concerning the $^4S_{3/2} \rightarrow ^4I_{15/2}$ transition, we obtained the following decay times : $\tau_1 = 24.42 \mu s$, $\tau_2 = 81.27 \mu s$ and $\tau_3 = 255.62 \mu s$ and concerning the $^4F_{9/2} \rightarrow ^4I_{15/2}$ transition, we obtained the following decay times : $\tau_1 = 34.25 \mu s$ and $\tau_2 = 518.79 \mu s$. The mean decay time is usually calculated with the (3) relation [53]. We obtained 163 μs and 481 μs for the $^4S_{3/2} \rightarrow ^4I_{15/2}$ and $^4F_{9/2} \rightarrow ^4I_{15/2}$ transitions, respectively. These values are in good agreement with measurements

of decay times performed on $\text{Lu}_2\text{O}_3:\text{Er}^{3+}$ [58]. The decay time for the $^4\text{S}_{3/2} \rightarrow ^4\text{I}_{15/2}$ obtained previously with UV excitation, 32.9 μs , is lower than the decay time determined for the same transition on the upconversion process. This high value found for the up-conversion process is a proof of the presence of an ET process and confirms the upconversion routes depicted in Figure 6 [58].

To complete this study, the fluorescence signature of the $\text{La}_{1.9}\text{Er}_{0.1}\text{Ti}_2\text{O}_7$ oxide was achieved via the measurements of Time-Resolved Emission Spectra (TRES). The outcome is a 3D surface allowing to follow the time evolution of the fluorescence as a function of the emission wavelength (Figure S2 – Supplementary Information). The main emission lies between 525 and 565 nm and the steady state spectrum ($I=f(\lambda_{\text{em}})$) shows the presence of multiple components in the decay of the transitions, as described above.

The upconversion process can be achieved over a wide spectral range. Indeed, we also carry out tests under a laser excitation at 785 nm. The pictures obtained are shown in Figure 8. For a low erbium ion content ($x = 0.01$), we can observe a yellow color due to a color superposition caused by the laser (red) scattering and by the upconversion effect with green emission. Between $x = 0.05$ and 0.30, the emission due to the upconversion property (green emission) completely dominates the laser scattering at the surface of the sample. Beyond $x = 0.50$, concentration quenching is observed for the upconversion process and the laser scattering at the surface of the sample takes the advantage. To finish, at $x = 1.8$, we observe, with the naked eye, only the scattering of the laser.

3.4 Thermal quenching of upconversion luminescence

The temperature-dependent upconversion emission spectra of $\text{La}_{1.90}\text{Er}_{0.10}\text{Ti}_2\text{O}_7$ specimen under laser excitation at 808 nm are shown in Figure 9a. The conventional emission spectra with the emission bands attributable to $^2\text{H}_{11/2} \rightarrow ^4\text{I}_{15/2}$, $^4\text{S}_{3/2} \rightarrow ^4\text{I}_{15/2}$ and $^4\text{F}_{9/2} \rightarrow ^4\text{I}_{15/2}$ transitions,

located at 520, 544 and 660 nm, respectively, are observed. In addition, three behaviors are observed depending on the nature of the transition. The intensity of $^4S_{3/2} \rightarrow ^4I_{15/2}$ transition increases from 77 to 150 K and then starts to decrease. The opposite is observed for the $^2H_{11/2} \rightarrow ^4I_{15/2}$ transition, where the weak intensity at ca. 520 nm appears only at 150 K. The change in intensities of $^2H_{11/2} \rightarrow ^4I_{15/2}$ and $^4S_{3/2} \rightarrow ^4I_{15/2}$ transitions are better seen in normalized (to 544 nm) temperature dependent upconversion emission spectra depicted in Figure 9b. It is obvious that the relative intensity of $^2H_{11/2} \rightarrow ^4I_{15/2}$ transition is constantly increasing with the temperature. The absence of $^2H_{11/2} \rightarrow ^4I_{15/2}$ transition at very low temperatures clearly shows that the $^2H_{11/2}$ level is only thermally populated from the lower $^4S_{3/2}$ level. The evolution of the mentioned transitions with the temperature are presented more clearly on the surface map (Figure 9c).

Since $^2H_{11/2}$ and $^4S_{3/2}$ levels are in thermal equilibrium, the electrons obey Boltzmann distribution law, therefore, the fluorescence intensity ratio (*FIR* or *R(T)*) I_H/I_S can be expressed by the following equation [59]:

$$R(T) = \frac{I_H}{I_S} = A \exp\left(\frac{-\Delta E}{k_B T}\right) \quad (4)$$

Here I_H and I_S are integrated intensities of $^2H_{11/2} \rightarrow ^4I_{15/2}$ and $^4S_{3/2} \rightarrow ^4I_{15/2}$ transitions, respectively. A is a constant, ΔE is the energy gap separating the $^2H_{11/2}$ and $^4S_{3/2}$ levels, k_B is the Boltzmann constant, and T is the absolute temperature. The calculated values of I_H/I_S as a function of temperature for $\text{La}_{1.90}\text{Er}_{0.10}\text{Ti}_2\text{O}_7$ sample are shown in Figure 10a. The fit of this experimentally obtained data with equation (4) yielded $\Delta E = 712 \pm 21 \text{ cm}^{-1}$ and $A = 20.73 \pm 1.44$. Temperature dependent fluorescence intensity ratio can be employed in thermal sensing, which provides a measure that is essentially independent from the excitation intensity fluctuations [60],[61]. The thermal sensing effect on the green upconversion fluorescence was also observed in our samples, where the intensity of $^2H_{11/2} \rightarrow ^4I_{15/2}$ and $^4S_{3/2} \rightarrow ^4I_{15/2}$ emissions varied with

the measurement temperature. For Er^{3+} -based temperature sensor, the sensitivity (S) can be defined as the change rate of $R(T)$ per unit temperature, which can be expressed as [62]:

$$S(T) = \frac{dR(T)}{dT} = A \exp\left(\frac{-\Delta E}{k_B T}\right) \left(\frac{\Delta E}{k_B T^2}\right) \quad (5)$$

Since the values of A and ΔE were already obtained from equation (4), it was possible to model the sensitivity curve, which is shown in Figure 10b. The sensitivity reaches a maximum of 0.011 K^{-1} at 512 K . However, sensitivity varies greatly with the temperature and can be rather low at lower temperatures, thus the temperature range for application is limited. **It is safe to account** that $\text{La}_{1.90}\text{Er}_{0.10}\text{Ti}_2\text{O}_7$ sample should be used in a temperature region where the sensitivity S is higher than half of its maximum value S_{Max} , as illustrated in Figure 10b. Therefore, the applicable sensing temperature should be higher than 250 K but lower than the sample synthesis temperature (1373 K) [63].

To check the ability of this compound for Optical Temperature sensors, the obtained values for S_{max} and T_{max} were compared to those reported on for some others systems [64],[65],[66],[67],[68],[69],[70] as shown in Table 1. The higher value for S_{max} was obtained for this studied phosphor powder. Furthermore, the range of use is relatively wide between 250 K and the synthesis temperature of the oxide, i.e. 1373 K . The results show that the $\text{La}_{1.9}\text{Er}_{0.1}\text{Ti}_2\text{O}_7$ oxide is well suitable for the conception of an optical temperature sensor.

For $^4\text{F}_{9/2} \rightarrow ^4\text{I}_{15/2}$ transition, a continuous decrease of the luminescence intensity according to the temperature is observed (Figure 11a). The reduction of luminescence with temperature is related to the enhancement of non-radiative transitions from excited state to ground state [71],[72]. The Mott-Seitz mechanism [72],[73] described this evolution where the luminescence intensity follows equation:

$$I(T) = \frac{I_0}{1 + C e^{-\frac{W}{k_B T}}} \quad (6)$$

Where, I_0 and $I(T)$ are the initial intensity and the intensity at T temperature, respectively. C is constant, k_B is Boltzmann's constant ($8.617 \cdot 10^{-5}$ eV/K) and W is thermal activation energy for the non-radiative transition. It is worth to notice that the phonon-assisted transitions are neglected in the luminescence decay relation. The activation energy can be easily obtained by plotting $\ln[(I_0/I)-1]$ versus $1/T$ [74], where a slope is equal to $-E_a/k_B$. For $^4F_{9/2} \rightarrow ^4I_{15/2}$ transition, the activation energy was found to be 18.4 ± 0.9 meV in $\text{La}_{1.9}\text{Er}_{0.1}\text{Ti}_2\text{O}_7$, as shown in the insert of Figure 11a.

For $^2H_{11/2} \rightarrow ^4I_{15/2}$ and $^4S_{3/2} \rightarrow ^4I_{15/2}$ transitions, the behaviors are different with an increase then a decrease in the intensity of luminescence emitted (Figure 11b). In this case, the luminescence emission is subject to both thermal assistance and thermal quenching. The maximum is reached for 150 and 450 K for $^4S_{3/2} \rightarrow ^4I_{15/2}$ and $^2H_{11/2} \rightarrow ^4I_{15/2}$ transitions, respectively.

Two assumptions can be made about the processes. The first hypothesis is the presence of oxygen vacancies. The electron is moving from the trap level to an oxygen vacancy level by thermal energy (the conduction band is located too high above the energy level of the oxygen vacancy trap to enable a thermally assisted transition to the conduction band). Subsequently, an energy transfer is carried out on Er^{3+} ions. This assumption requires close proximity of the vacancies to the luminescent centers. This model is already proposed by Aitasalo *et al.* for $\text{CaAl}_2\text{O}_4:\text{Eu}^{2+}$ [75]. The second hypothesis is the presence of several trap levels close to the $^4S_{3/2}$ and $^2H_{11/2}$ levels. Thus, the electrons could pass on these levels by thermal stimulation ($k_B T$) and then come to populate the levels by quantum tunneling. These mechanisms can also explain the fact that the intensity of luminescence of the $^4F_{9/2} \rightarrow ^4I_{15/2}$ transition decreases as a function of temperature without passing through a maximum. This appears because the energy trap levels are too far from the transition and the transition is not allowed.

The CIE 1931 Chromaticity coordinates of $\text{La}_{1.9}\text{Er}_{0.1}\text{Ti}_2\text{O}_7$ vs. temperature are illustrated in Figure 12. We do not observe a linear evolution in the whole 77 – 500 K temperature range due to the presence of a competition between the thermal quenching and the thermal assistance effects. Nevertheless, two linear evolutions are revealed with a break around 150 K. The shift of the color coordinates towards greener region goes hand in hand with the increasing relative intensity of higher energy $^2\text{H}_{11/2} \rightarrow ^4\text{I}_{15/2}$ transition at elevated temperatures, as was already demonstrated in Figure 9b. These results show that $\text{La}_{1.9}\text{Er}_{0.1}\text{Ti}_2\text{O}_7$ can be used as an optical temperature sensor [76] based on the upconversion luminescence of Er^{3+} with higher sensitivity and good resolution. Moreover, as described above, the UC emission is observed over a wide excitation range from 785 to 980 nm. This wide range of use is advantageous, particularly for applications in phototherapy or for photovoltaic applications.

4. Conclusion

The classical and upconversion luminescence properties of $\text{La}_{2-x}\text{Er}_x\text{Ti}_2\text{O}_7$ oxides, synthesized by solid-state reaction, have been studied. The structural characterization performed by X-ray diffraction have shown that a partial solid solution with monoclinic/layered-perovskite structure can be obtained until $x = 0.10$. Beyond, a bi-phasic mixture containing a layered perovskite phase and pyrochlore phase ($\text{Er}_2\text{Ti}_2\text{O}_7$) was obtained. The luminescence properties based on emission and excitation spectra, fluorescence lifetime, quantum efficiency were discussed. The maximum intensity of luminescence under excitation at 377 nm is obtained for $x = 0.10$. These oxides also exhibit UC properties over a wide spectral range (785 to 980 nm). This may represent an advantage for various applications in phototherapy or even in photovoltaic cells in order to adapt the spectrum to the best response of the cell. The laser power dependence is the proof of two-photon absorption process in the case of green and red emissions, and lifetime studies indicate a process involving an energy

transfer between two ions. From these results, mechanisms have been described to explain the upconversion process. The temperature dependence of the UC luminescence was also investigated in this work. With increasing temperature, the $^4F_{9/2} \rightarrow ^4I_{15/2}$ intensity of the transition decreases according to the Mott-Seitz law whose activation energy is 18.4 meV. For $^2H_{11/2} \rightarrow ^4I_{15/2}$ and $^4S_{3/2} \rightarrow ^4I_{15/2}$ transitions, the intensity passes through a maximum indicating a phenomenon of thermal assistance. The intensity variation was modeled and it shown two different behaviors depending on the transition type. To finish, the CIE 1931 chromaticity coordinates of $\text{La}_{1.9}\text{Er}_{0.1}\text{Ti}_2\text{O}_7$ as function of the temperature were calculated. The results indicate an interesting color balance due to thermal assistance phenomena allowing use of synthesized material as a temperature sensor.

Acknowledgements

The work was financially supported by the PHC Gilibert (N° 373027ZC) and Research Council of Lithuania (No. S-LZ-17-4/LSS-610000-2007). Chevreul Institute (FR 2638)", "Ministère de l'Enseignement Supérieur et de la Recherche", "Région Nord Pas-de-Calais", "FEDER" and "C'Nano Nord-Ouest competence centre" are also acknowledged for supporting and funding this work. N. Kania is thanked for his help in TGA experiments.

References

- [1] N. Bloembergen, Solid State Infrared Quantum Counters, *Phys. Rev. Lett.* 2 (1959) 84–85. doi:10.1103/PhysRevLett.2.84.
- [2] F. Auzel, Compteur quantique par transfert d'énergie entre deux ions de terres rares dans un tungstate mixte et dans un verre, (1966) 1016–1019.
- [3] V.V. Ovsyankin, P.P. Feofilov, *JETP Letters*, 3 12 (1966) 322.
- [4] R. Scheps, Upconversion laser processes, *Prog. Quantum Electron.* 20 (1996) 271–358. doi:10.1016/0079-6727(95)00007-0.
- [5] P. Du, L. Luo, W. Li, Q. Yue, H. Chen, Optical temperature sensor based on upconversion emission in Er-doped ferroelectric $0.5\text{Ba}(\text{Zr}_{0.2}\text{Ti}_{0.8})\text{O}_3$ - $0.5(\text{Ba}_{0.7}\text{Ca}_{0.3})\text{TiO}_3$ ceramic, *Appl. Phys. Lett.* 104 (2014) 152902. doi:10.1063/1.4871378.
- [6] E.P. Schartner, D. Jin, H. Ebendorff-Heidepriem, J.A. Piper, Z. Lu, T.M. Monro, Lanthanide upconversion within microstructured optical fibers: improved detection limits

- for sensing and the demonstration of a new tool for nanocrystal characterization, *Nanoscale*. 4 (2012) 7448–7451. doi:10.1039/C2NR32583G.
- [7] F. Wang, X. Liu, Recent advances in the chemistry of lanthanide-doped upconversion nanocrystals, *Chem. Soc. Rev.* 38 (2009) 976–989. doi:10.1039/B809132N.
- [8] H. Zhong, Z. Wang, W. Lu, J. Liu, Y. Wang, Luminescent Materials for 3D Display Technology, in: R.-S. Liu (Ed.), *Phosphors Convers. Nano Part. Quantum Dots Their Appl.*, Springer Singapore, 2016: pp. 503–523. doi:10.1007/978-981-10-1590-8_18.
- [9] P. Alonso-Cristobal, O. Oton-Fernandez, D. Mendez-Gonzalez, J.F. Díaz, E. Lopez-Cabarcos, I. Barasoain, J. Rubio-Retama, Synthesis, Characterization, and Application in HeLa Cells of an NIR Light Responsive Doxorubicin Delivery System Based on NaYF₄:Yb,Tm@SiO₂-PEG Nanoparticles, *ACS Appl. Mater. Interfaces*. 7 (2015) 14992–14999. doi:10.1021/acsami.5b03881.
- [10] F. Wang, D. Banerjee, Y. Liu, X. Chen, X. Liu, Upconversion nanoparticles in biological labeling, imaging, and therapy, *The Analyst*. 135 (2010) 1839–1854. doi:10.1039/c0an00144a.
- [11] C.T. Xu, Q. Zhan, H. Liu, G. Somesfalean, J. Qian, S. He, S. Andersson-Engels, Upconverting nanoparticles for pre-clinical diffuse optical imaging, microscopy and sensing: Current trends and future challenges, *Laser Photonics Rev.* 7 (2013) 663–697. doi:10.1002/lpor.201200052.
- [12] D. Mendez-Gonzalez, E. Lopez-Cabarcos, J. Rubio-Retama, M. Laurenti, Sensors and bioassays powered by upconverting materials, *Adv. Colloid Interface Sci.* (2017) In press. doi:10.1016/j.cis.2017.06.003.
- [13] M. Lin, Y. Gao, F. Hornicek, F. Xu, T.J. Lu, M. Amiji, Z. Duan, Near-infrared light activated delivery platform for cancer therapy, *Adv. Colloid Interface Sci.* 226 (2015) 123–137. doi:10.1016/j.cis.2015.10.003.
- [14] M. Kamimura, A. Omoto, H.-C. Chiu, K. Soga, Enhanced Red Upconversion Emission of NaYF₄:Yb³⁺, Er³⁺, Mn²⁺ Nanoparticles for Near-Infrared Induced Photodynamic Therapy and Fluorescence Imaging, *Chem. Lett.* (2017). doi:10.1246/cl.170322.
- [15] V.M. Lojpur, P.S. Ahrenkiel, M.D. Dramićanin, Color-tunable up-conversion emission in Y₂O₃:Yb³⁺, Er³⁺ nanoparticles prepared by polymer complex solution method, *Nanoscale Res. Lett.* 8 (2013) 131. doi:10.1186/1556-276X-8-131.
- [16] J. Zhou, Q. Liu, W. Feng, Y. Sun, F. Li, Upconversion luminescent materials: advances and applications, *Chem. Rev.* 115 (2015) 395–465. doi:10.1021/cr400478f.
- [17] S. Saitzek, Z. Shao, A. Bayart, P. Roussel, R. Desfeux, Microstructure and Nanoscale Piezoelectric/Ferroelectric Properties in Ln₂Ti₂O₇ (Ln= Lanthanide) Thin Films with Layered Perovskite Structure, in: P. Granger, V.I. Parvulescu, V.I. Parvulescu, W. Prellier (Eds.), *Perovskites Relat. Mix. Oxides*, Wiley-VCH Verlag GmbH & Co. KGaA, 2016: pp. 233–258. <http://onlinelibrary.wiley.com/doi/10.1002/9783527686605.ch11/summary> (accessed January 6, 2017).
- [18] Z. Shao, S. Saitzek, P. Roussel, A. Ferri, O. Mentré, R. Desfeux, Investigation of microstructure in ferroelectric lead-free La₂Ti₂O₇ thin film grown on (001)-SrTiO₃ substrate, *CrystEngComm*. 14 (2012) 6524–6533. doi:10.1039/C2CE26078F.
- [19] M. Kimura, S. Nanamatsu, K. Doi, S. Matsushita, M. Takahashi, Electrooptic and Piezoelectric Properties of La₂Ti₂O₇ Single Crystal, *Jpn. J. Appl. Phys.* 11 (1972) 904–904. doi:10.1143/JJAP.11.904.
- [20] A. Sayir, S.C. Farmer, F. Dynys, High Temperature Piezoelectric La₂Ti₂O₇, in: F. Dogan, P. Kumta (Eds.), *Adv. Electron. Electrochem. Ceram.*, John Wiley & Sons, Inc., 2006: pp. 57–68. doi:10.1002/9781118407899.ch6.

- [21] H.G. Kim, D.W. Hwang, S.W. Bae, J.H. Jung, J.S. Lee, Photocatalytic Water Splitting over $\text{La}_2\text{Ti}_2\text{O}_7$ Synthesized by the Polymerizable Complex Method, *Catal. Lett.* 91 (2003) 193–198. doi:10.1023/B:CATL.0000007154.30343.23.
- [22] D.W. Hwang, K.Y. Cha, J. Kim, H.G. Kim, S.W. Bae, J.S. Lee, Photocatalytic Degradation of CH_3Cl over a Nickel-Loaded Layered Perovskite, *Ind. Eng. Chem. Res.* 42 (2003) 1184–1189. doi:10.1021/ie020457c.
- [23] P.T. Diallo, P. Boutinaud, R. Mahiou, Anti-Stokes luminescence and site selectivity in $\text{La}_2\text{Ti}_2\text{O}_7:\text{Pr}^{3+}$, *J. Alloys Compd.* 341 (2002) 139–143. doi:10.1016/S0925-8388(02)00098-1.
- [24] Z. Shao, S. Saitzek, J.-F. Blach, A. Sayede, P. Roussel, R. Desfeux, Structural Characterization and Photoluminescent Properties of $(\text{La}_{1-x}\text{Sm}_x)_2\text{Ti}_2\text{O}_7$ Solid Solutions Synthesized by a Sol–Gel Route, *Eur. J. Inorg. Chem.* 2011 (2011) 3569–3576. doi:10.1002/ejic.201100309.
- [25] A. Bayart, A. Katelnikovas, J.-F. Blach, J. Rousseau, S. Saitzek, Synthesis, structural and luminescence properties of $(\text{La}_{1-x}\text{Ln}_x)_2\text{Ti}_2\text{O}_7$ (Ln =lanthanides) solid solutions, *J. Alloys Compd.* 683 (2016) 634–646. doi:10.1016/j.jallcom.2016.05.041.
- [26] X. Li, H. Cai, L. Ding, X. Dou, W. Zhang, Synthesis and luminescence properties of $\text{La}_2\text{Ti}_2\text{O}_7:\text{Er}^{3+}$ nanocrystals with pyrochlore structure, *J. Alloys Compd.* 541 (2012) 36–40. doi:10.1016/j.jallcom.2012.07.017.
- [27] A. Ferri, S. Saitzek, Z. Shao, G. Declercq, J. Costecalde, D. Rémiens, D. Deresmes, D. Troadec, R. Desfeux, Ion-Beam Etching on Nanostructured $\text{La}_2\text{Ti}_2\text{O}_7$ Piezoelectric Thin Films, *J. Am. Ceram. Soc.* 96 (2013) 3877–3882. doi:10.1111/jace.12626.
- [28] Y. Zhang, V. Shutthanandan, R. Devanathan, S. Thevuthasan, D.E. McCready, J. Young, G. Balakrishnan, D.M. Paul, W.J. Weber, Damage accumulation and amorphization in samarium titanate pyrochlore, *Nucl. Instrum. Methods Phys. Res. Sect. B Beam Interact. Mater. At.* 218 (2004) 89–94. doi:10.1016/j.nimb.2003.12.003.
- [29] F. Lichtenberg, A. Herrnberger, K. Wiedenmann, J. Mannhart, Synthesis of perovskite-related layered $\text{A}_n\text{B}_n\text{O}_{3n+2} = \text{ABO}_x$ type niobates and titanates and study of their structural, electric and magnetic properties, *Prog. Solid State Chem.* 29 (2001) 1–70. doi:10.1016/S0079-6786(01)00002-4.
- [30] M. Gasperin, Ditungstate de lanthane, *Acta Crystallogr. B.* 31 (1975) 2129–2130. doi:10.1107/S0567740875007005.
- [31] M. Tanaka, H. Sekii, K. Ohi, Structural Study of $\text{La}_2\text{Ti}_2\text{O}_7$ by Convergent-Beam Electron Diffraction and Electron Microscopy, *Jpn. J. Appl. Phys.* 24 (1985) 814. doi:10.7567/JJAPS.24S2.814.
- [32] P.A. Fuierer, R.E. Newnham, $\text{La}_2\text{Ti}_2\text{O}_7$ Ceramics, *J. Am. Ceram. Soc.* 74 (1991) 2876–2881. doi:10.1111/j.1151-2916.1991.tb06857.x.
- [33] V.V. Atuchin, T.A. Gavrilova, J.-C. Grivel, V.G. Kesler, Electronic structure of layered ferroelectric high- k titanate $\text{La}_2\text{Ti}_2\text{O}_7$, *J. Phys. Appl. Phys.* 42 (2009) 035305. doi:10.1088/0022-3727/42/3/035305.
- [34] D.S. Todorovsky, R.V. Todorovska, M.M. Milanova, D.G. Kovacheva, Deposition and characterization of $\text{La}_2\text{Ti}_2\text{O}_7$ thin films via spray pyrolysis process, *Appl. Surf. Sci.* 253 (2007) 4560–4565. doi:10.1016/j.apsusc.2006.10.016.
- [35] A.V. Prasadaraio, U. Selvaraj, S. Komarneni, A.S. Bhalla, Fabrication of $\text{La}_2\text{Ti}_2\text{O}_7$ thin films by a sol-gel technique, *Ferroelectr. Lett. Sect.* 14 (1992) 65–72. doi:10.1080/07315179208203344.
- [36] H. Song, T. Peng, P. Cai, H. Yi, C. Yan, Hydrothermal synthesis of flaky crystallized $\text{La}_2\text{Ti}_2\text{O}_7$ for producing hydrogen from photocatalytic water splitting, *Catal. Lett.* 113 (2007) 54–58. doi:10.1007/s10562-006-9004-6.

- [37] Z. Zhao, Y. Zhang, J. Yang, H. Li, W. Song, X. Zhao, J. Ceram. Soc. Jpn. 113 (2005) 67–70. doi:10.2109/jcersj.113.67.
- [38] M. Suresh, A.V. Prasadaraao, S. Komarneni, Mixed Hydroxide Precursors for $\text{La}_2\text{Ti}_2\text{O}_7$ and $\text{Nd}_2\text{Ti}_2\text{O}_7$ by Homogeneous Precipitation, J. Electroceramics. 6 (2001) 147–151. doi:10.1023/A:1011464902626.
- [39] S. Nanamatsu, M. Kimura, K. Doi, S. Matsushita, N. Yamada, A new ferroelectric: $\text{La}_2\text{Ti}_2\text{O}_7$, Ferroelectrics. 8 (1974) 511–513. doi:10.1080/00150197408234143.
- [40] J. Tauc, Optical properties and electronic structure of amorphous Ge and Si, Mater. Res. Bull. 3 (1968) 37–46. doi:10.1016/0025-5408(68)90023-8.
- [41] R. Castañeda, E. Chavira, O. Peralta, Product Prediction: Intermediates Formed During Rare Earth Reactions, J. Mex. Chem. Soc. 58 (2014) 82–87.
- [42] B. Bakiz, F. Guinneton, M. Arab, A. Benlhachemi, S. Villain, P. Satre, J.-R. Gavarri, Carbonatation and Decarbonatation Kinetics in the La_2O_3 - $\text{La}_2\text{O}_2\text{CO}_3$ System under CO_2 Gas Flows, Adv. Mater. Sci. Eng. 2010 (2010) e360597. doi:10.1155/2010/360597.
- [43] E. Füglein, D. Walter, Thermal behaviour of lanthanum hydroxide in dependency of pressure, Z. Für Anorg. Allg. Chem. 632 (2006) 2154–2154. doi:10.1002/zaac.200670155.
- [44] F.X. Zhang, J. Lian, U. Becker, R.C. Ewing, L.M. Wang, J. Hu, S.K. Saxena, Structural change of layered perovskite $\text{La}_2\text{Ti}_2\text{O}_7$ at high pressures, J. Solid State Chem. 180 (2007) 571–576. doi:10.1016/j.jssc.2006.11.022.
- [45] G.H. Dieke, H.M. Crosswhite, H. Crosswhite, Spectra and energy levels of rare earth ions in crystals, Interscience Publishers, New York, 1968.
- [46] L. Tian, Z. Xu, S. Zhao, Y. Cui, Z. Liang, J. Zhang, X. Xu, The Upconversion Luminescence of $\text{Er}^{3+}/\text{Yb}^{3+}/\text{Nd}^{3+}$ Triply-Doped $\beta\text{-NaYF}_4$ Nanocrystals under 808-nm Excitation, Materials. 7 (2014) 7289–7303. doi:10.3390/ma7117289.
- [47] Y. Liu, Y. Liu, G. Liu, X. Dong, J. Wang, Up/down conversion, tunable photoluminescence and energy transfer properties of $\text{NaLa}(\text{WO}_4)_2:\text{Er}^{3+}, \text{Eu}^{3+}$ phosphors, RSC Adv. 5 (2015) 97995–98003. doi:10.1039/C5RA17370A.
- [48] J. Rocha, L.D. Carlos, J.P. Rainho, Z. Lin, P. Ferreira, R.M. Almeida, Photoluminescence of new Er^{3+} -doped titanosilicate materials, J. Mater. Chem. 10 (2000) 1371–1375. doi:10.1039/A910192F.
- [49] G. Blasse, Energy transfer in oxidic phosphors, Phys. Lett. A. 28 (1968) 444–445. doi:10.1016/0375-9601(68)90486-6.
- [50] M. Xu, L. Wang, D. Jia, H. Zhao, Tuning the Color Emission of $\text{Sr}_2\text{P}_2\text{O}_7:\text{Tb}^{3+}, \text{Eu}^{3+}$ Phosphors Based on Energy Transfer, J. Am. Ceram. Soc. 98 (2015) 1536–1541. doi:10.1111/jace.13497.
- [51] J.R. Lakowicz, Principles of Fluorescence Spectroscopy, Springer Science & Business Media, 2007.
- [52] L. Li, C. Guo, S. Jiang, D.K. Agrawal, T. Li, Green up-conversion luminescence of Yb^{3+} - Er^{3+} co-doped $\text{CaLa}_2\text{ZnO}_5$ for optically temperature sensing, RSC Adv. 4 (2014) 6391–6396. doi:10.1039/C3RA47264G.
- [53] A. Sillen, Y. Engelborghs, The Correct Use of “Average” Fluorescence Parameters, Photochem. Photobiol. 67 (1998) 475–486. doi:10.1111/j.1751-1097.1998.tb09082.x.
- [54] J. Castañeda, Saturation effect of up-conversion luminescence from erbium-doped, silica-titania sol-gel powders, J. Rare Earths. 29 (2011) 420–425. doi:10.1016/S1002-0721(10)60472-3.
- [55] J.A. Capobianco, G. Prevost, P.P. Proulx, P. Kabro, M. Bettinelli, Upconversion properties of Er^{3+} doped lead silicate glasses, Opt. Mater. 6 (1996) 175–184. doi:10.1016/0925-3467(96)00031-6.
- [56] L. Pihlgren, T. Laihin, L.C.V. Rodrigues, S. Carlson, K.O. Eskola, A. Kotlov, M. Lastusaari, T. Soukka, H.F. Brito, J. Hölsä, On the mechanism of persistent up-conversion

- luminescence in the $\text{ZrO}_2\text{:Yb}^{3+},\text{Er}^{3+}$ nanomaterials, *Opt. Mater.* 36 (2014) 1698–1704. doi:10.1016/j.optmat.2014.01.027.
- [57] B. Henke, F. Pientka, J.A. Johnson, B. Ahrens, P.T. Miclea, S. Schweizer, Saturation effects in the upconversion efficiency of Er-doped fluorozirconate glasses, *J. Phys. Condens. Matter.* 22 (2010) 155107. doi:10.1088/0953-8984/22/15/155107.
- [58] F. Vetrone, J.C. Boyer, J.A. Capobianco, A. Speghini, M. Bettinelli, NIR to Visible Upconversion in Nanocrystalline and Bulk $\text{Lu}_2\text{O}_3\text{:Er}^{3+}$, *J. Phys. Chem. B.* 106 (2002) 5622–5628. doi:10.1021/jp020256m.
- [59] X. Wang, X. Kong, Y. Yu, Y. Sun, H. Zhang, Effect of Annealing on Upconversion Luminescence of ZnO:Er^{3+} Nanocrystals and High Thermal Sensitivity, *J. Phys. Chem. C.* 111 (2007) 15119–15124. doi:10.1021/jp0686689.
- [60] F. Sidirolou, S.A. Wade, N.M. Dragomir, G.W. Baxter, S.F. Collins, Effects of high-temperature heat treatment on Nd^{3+} -doped optical fibers for use in fluorescence intensity ratio based temperature sensing, *Rev. Sci. Instrum.* 74 (2003) 3524–3530. doi:10.1063/1.1578706.
- [61] S.A. Wade, S.F. Collins, G.W. Baxter, Fluorescence intensity ratio technique for optical fiber point temperature sensing, *J. Appl. Phys.* 94 (2003) 4743–4756. doi:10.1063/1.1606526.
- [62] X. Li, X. Wang, H. Zhong, L. Cheng, S. Xu, J. Sun, J. Zhang, X. Li, L. Tong, B. Chen, Effects of Er^{3+} concentration on down-/up-conversion luminescence and temperature sensing properties in $\text{NaGdTiO}_4\text{:Er}^{3+}/\text{Yb}^{3+}$ phosphors, *Ceram. Int.* 42 (2016) 14710–14715. doi:10.1016/j.ceramint.2016.06.096.
- [63] J. Li, J. Sun, J. Liu, X. Li, J. Zhang, Y. Tian, S. Fu, L. Cheng, H. Zhong, H. Xia, B. Chen, Pumping-route-dependent concentration quenching and temperature effect of green up- and down-conversion luminescence in $\text{Er}^{3+}/\text{Yb}^{3+}$ co-doped $\text{Gd}_2(\text{WO}_4)_3$ phosphors, *Mater. Res. Bull.* 48 (2013) 2159–2165. doi:10.1016/j.materresbull.2013.02.009.
- [64] S.F. León-Luis, U.R. Rodríguez-Mendoza, E. Lalla, V. Lavín, Temperature sensor based on the Er^{3+} green upconverted emission in a fluorotellurite glass, *Sens. Actuators B Chem.* 158 (2011) 208–213. doi:10.1016/j.snb.2011.06.005.
- [65] R. Balda, N. Hakmeh, M. Barredo-Zuriarrain, O. Merdrignac-Conanec, S. García-Revilla, M.A. Arriandaga, J. Fernández, Influence of Upconversion Processes in the Optically-Induced Inhomogeneous Thermal Behavior of Erbium-Doped Lanthanum Oxyulfide Powders, *Materials.* 9 (2016) 353. doi:10.3390/ma9050353.
- [66] F. CHI, F. HU, X. WEI, Y. CHEN, M. YIN, Synthesis and thermometric properties of $\text{Yb}^{3+}\text{-Er}^{3+}$ co-doped K_2GdF_5 up-conversion phosphors, *J. Rare Earths.* 35 (2017) 436–440. doi:10.1016/S1002-0721(17)60930-X.
- [67] D. Chen, Z. Wan, Y. Zhou, P. Huang, J. Zhong, M. Ding, W. Xiang, X. Liang, Z. Ji, Bulk glass ceramics containing $\text{Yb}^{3+}/\text{Er}^{3+}$: $\beta\text{-NaGdF}_4$ nanocrystals: Phase-separation-controlled crystallization, optical spectroscopy and upconverted temperature sensing behavior, *J. Alloys Compd.* 638 (2015) 21–28. doi:10.1016/j.jallcom.2015.02.170.
- [68] C. Li, B. Dong, C. Ming, M. Lei, Application to Temperature Sensor Based on Green Up-conversion of Er^{3+} Doped Silicate Glass, *Sensors.* 7 (2007) 2652–2659. doi:10.3390/s7112652.
- [69] Optical Thermometry through Green Upconversion Emissions in $\text{Er}^{3+}/\text{Yb}^{3+}$ -Codoped CaWO_4 Phosphor, *Appl. Phys. Express.* 5 (2012) 072201. doi:10.1143/APEX.5.072201.
- [70] B.P. Singh, A.K. Parchur, R.S. Ningthoujam, P.V. Ramakrishna, S. Singh, P. Singh, S.B. Rai, R. Maalej, Enhanced up-conversion and temperature-sensing behaviour of Er^{3+} and Yb^{3+} co-doped $\text{Y}_2\text{Ti}_2\text{O}_7$ by incorporation of Li^+ ions, *Phys. Chem. Chem. Phys.* 16 (2014) 22665–22676. doi:10.1039/C4CP02949F.

- [71] X. Cai, J.E. Martin, L.E. Shea-Rohwer, K. Gong, D.F. Kelley, Thermal Quenching Mechanisms in II–VI Semiconductor Nanocrystals, *J. Phys. Chem. C*. 117 (2013) 7902–7913. doi:10.1021/jp400688g.
- [72] D.W. Cooke, B.L. Bennett, R.E. Muenchausen, J.-K. Lee, M.A. Nastasi, Intrinsic ultraviolet luminescence from Lu_2O_3 , Lu_2SiO_5 and $\text{Lu}_2\text{SiO}_5:\text{Ce}^{3+}$, *J. Lumin.* 106 (2004) 125–132. doi:10.1016/j.jlumin.2003.09.001.
- [73] M.D. Dramićanin, Sensing temperature via downshifting emissions of lanthanide-doped metal oxides and salts. A review, *Methods Appl. Fluoresc.* 4 (2016) 042001. doi:10.1088/2050-6120/4/4/042001.
- [74] Y. Zhang, W. Gong, G. Ning, Novel red-emitting $\text{LiGd}(\text{WO}_4)_2:\text{Eu}^{3+}$ phosphor with high thermal stability and high color purity for application in white light-emitting diodes, *New J. Chem.* 40 (2016) 10136–10143. doi:10.1039/C6NJ02734B.
- [75] T. Aitasalo, P. Dereń, J. Hölsä, H. Jungner, J.-C. Krupa, M. Lastusaari, J. Legendziewicz, J. Niittykoski, W. Stręk, Persistent luminescence phenomena in materials doped with rare earth ions, *J. Solid State Chem.* 171 (2003) 114–122. doi:10.1016/S0022-4596(02)00194-9.
- [76] W. Xu, X. Gao, L. Zheng, Z. Zhang, W. Cao, An optical temperature sensor based on the upconversion luminescence from $\text{Tm}^{3+}/\text{Yb}^{3+}$ codoped oxyfluoride glass ceramic, *Sens. Actuators B Chem.* 173 (2012) 250–253. doi:10.1016/j.snb.2012.07.009.

FIGURES CAPTIONS

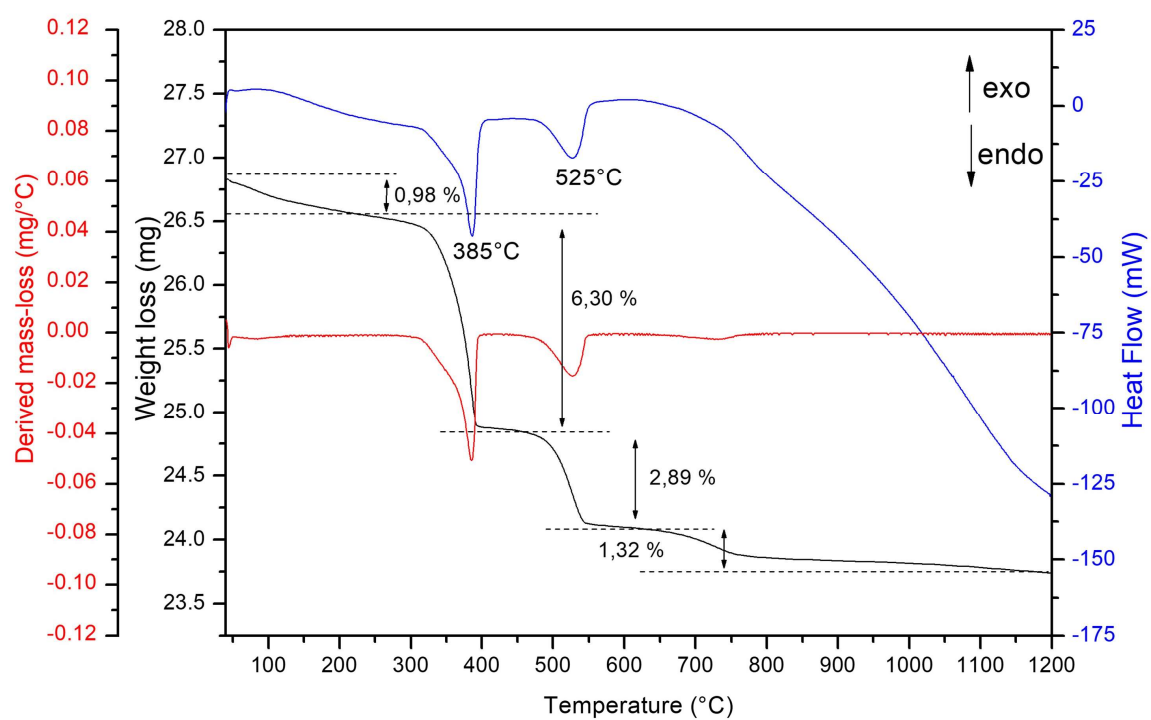


Figure 1. The TGA-DTA curves obtained on starting precursors in air.

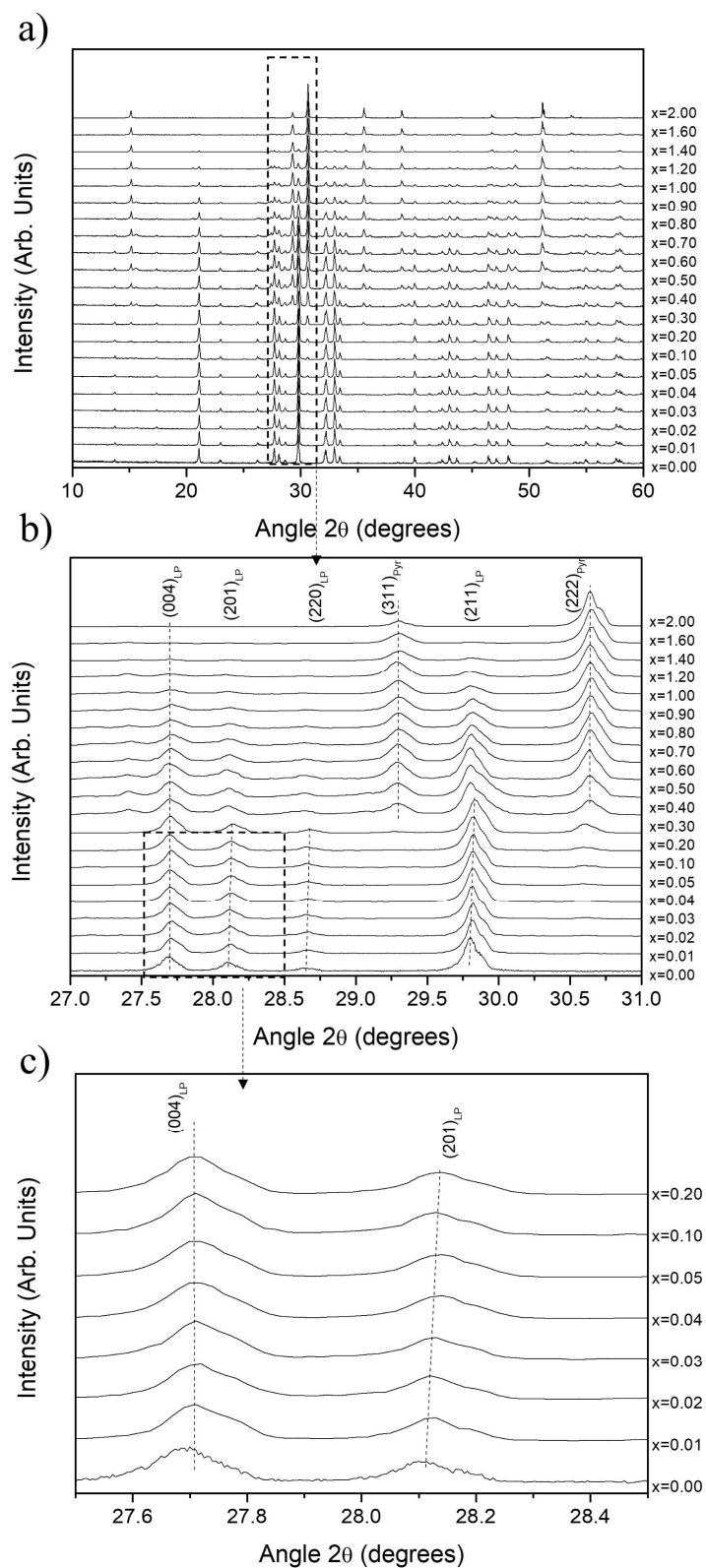


Figure 2. a) XRD patterns of $\text{La}_{2-x}\text{Er}_x\text{Ti}_2\text{O}_7$ powders according to x values; b) Zoom in the range of 27° to 31° ; c) XRD patterns zoomed in the range 27.5° to 28.5° .

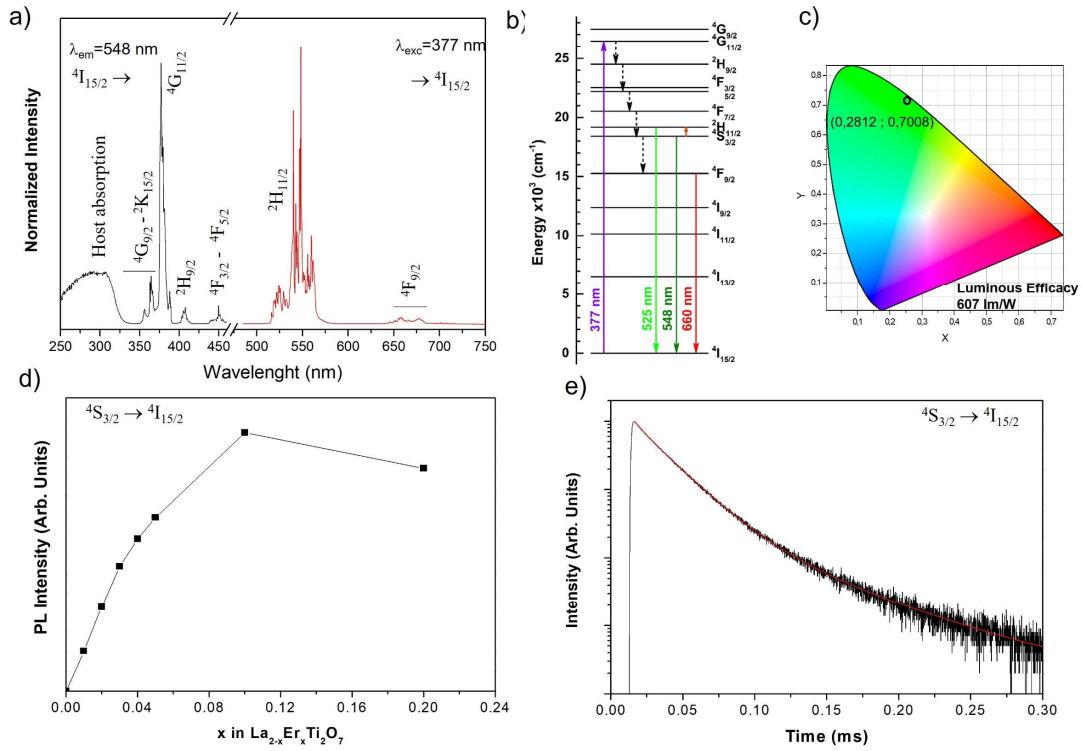


Figure 3. a) Excitation and emission spectra of $\text{La}_{1.9}\text{Er}_{0.1}\text{Ti}_2\text{O}_7$ recorded at room-temperature; b) Partial energy level structure of Er^{3+} ions; c) CIE 1931 chromaticity diagram with the coordinates of $\text{La}_{1.9}\text{Eu}_{0.1}\text{Ti}_2\text{O}_7$ samples d) Luminescence intensity evolution of $\text{La}_{2-x}\text{Er}_x\text{Ti}_2\text{O}_7$ as function of x values and e) Fluorescence decay curves ($\lambda_{\text{ex}} = 377$ nm, $\lambda_{\text{em}} = 548$ nm) of $\text{La}_{1.9}\text{Eu}_{0.1}\text{Ti}_2\text{O}_7$ (Theoretical double exponential fit is presented in red).

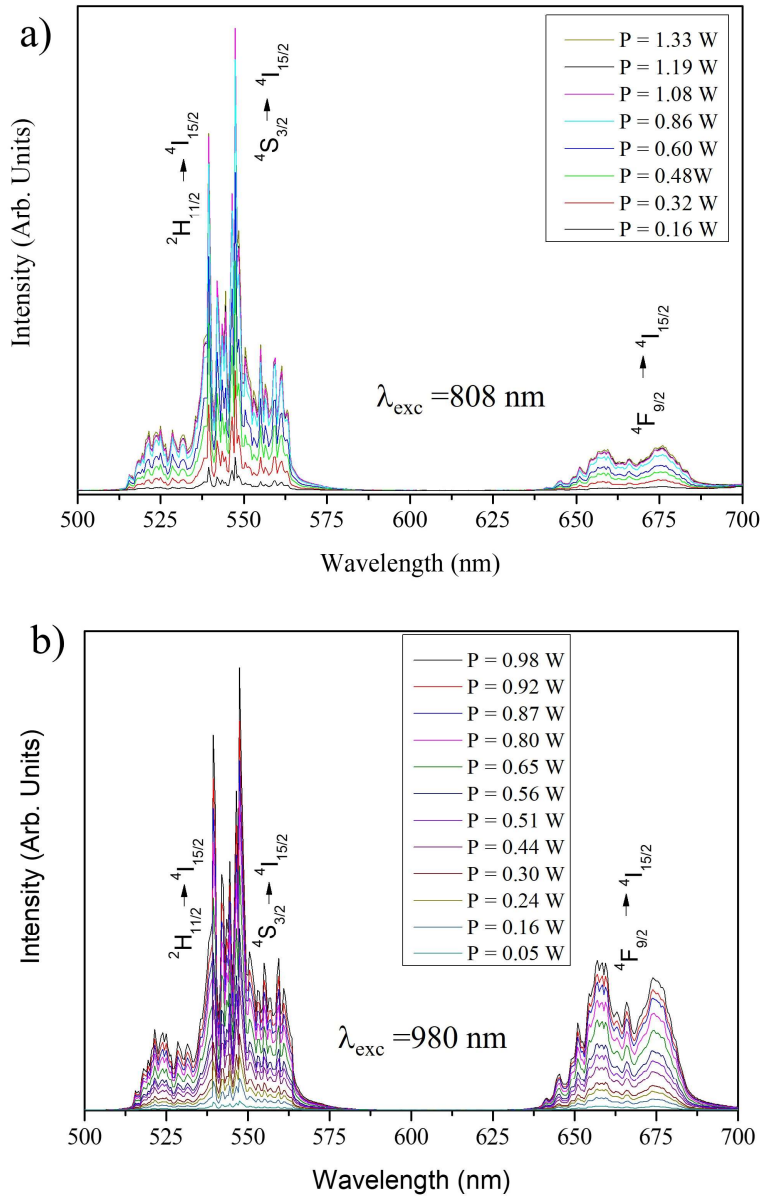


Figure 4. a) Upconversion emission spectra of $\text{La}_{1.9}\text{Er}_{0.1}\text{Ti}_2\text{O}_7$ ($\lambda_{\text{ex}} = 808 \text{ nm}$) at different laser power (from 0.16 to 1.33 W) recorded at room temperature; b) Upconversion emission spectra of $\text{La}_{1.9}\text{Er}_{0.1}\text{Ti}_2\text{O}_7$ ($\lambda_{\text{ex}} = 980 \text{ nm}$) at different laser power (from 0.05 to 0.98 W) recorded at room temperature.

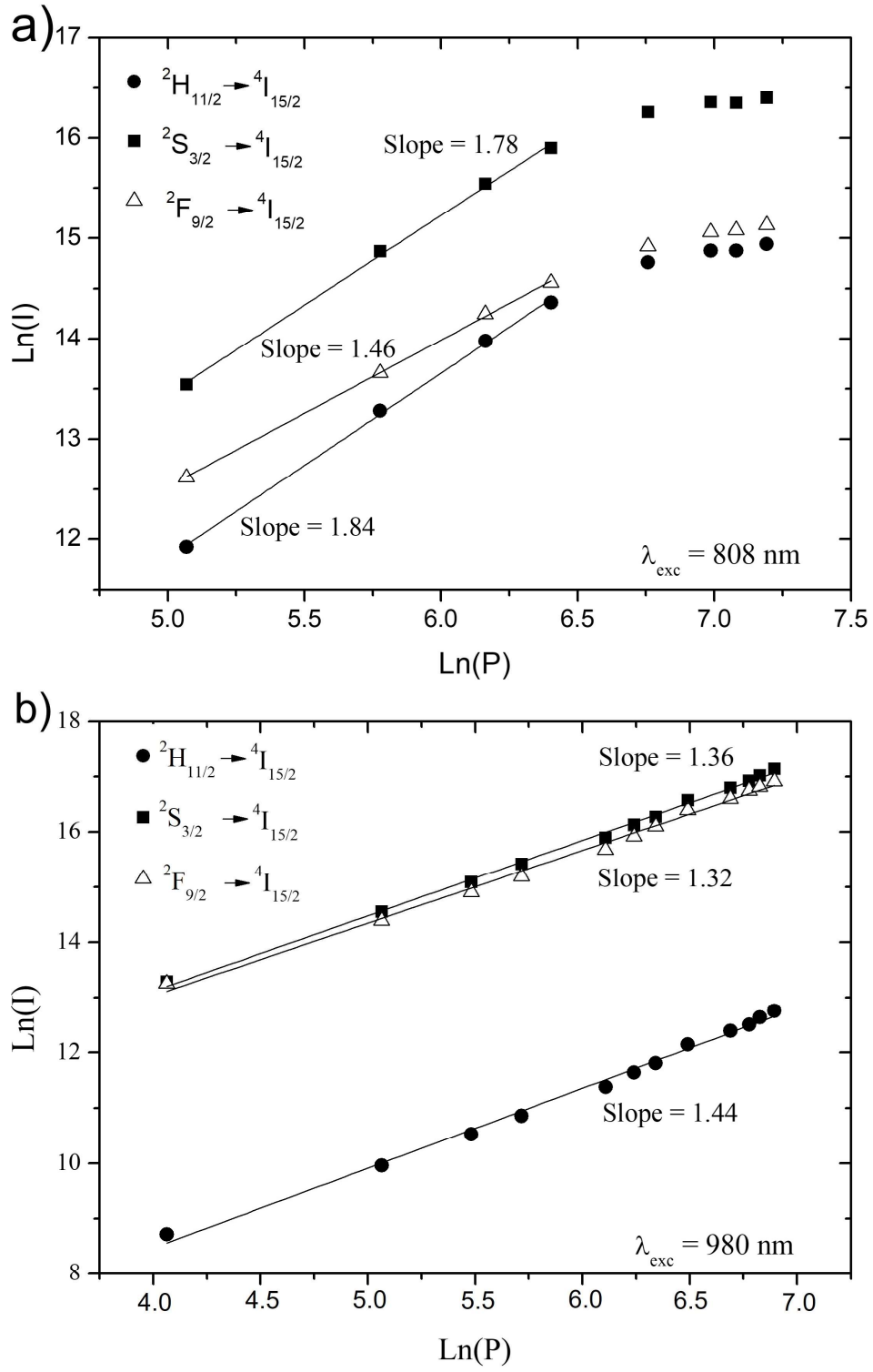


Figure 5. Power dependence of upconversion luminescence from ${}^2H_{11/2} \rightarrow {}^4I_{15/2}$, ${}^4S_{3/2} \rightarrow {}^4I_{15/2}$ and ${}^4S_{3/2} \rightarrow {}^4I_{15/2}$ in $\text{La}_{1.90}\text{Er}_{0.10}\text{Ti}_2\text{O}_7$ with two exciting lasers (808 (a) and 980 nm (b)).

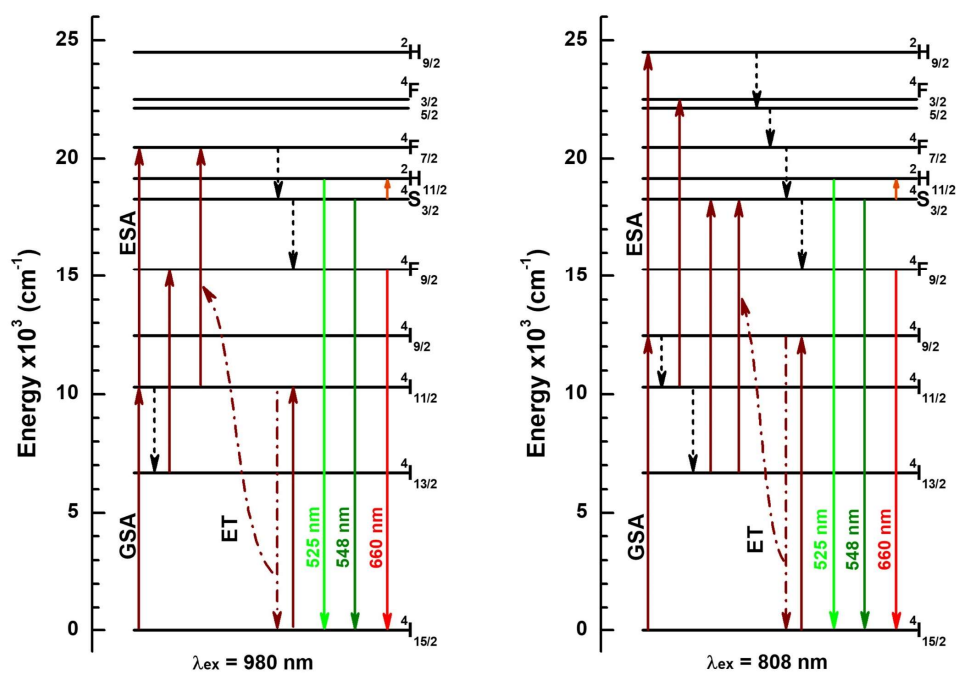


Figure 6. Energy diagram level of Er^{3+} . Possible ways of upconversion are described as ET (energy transfer between two ions) and ESA (excited-state absorption) for an excitation at 980 and 808 nm. Solid arrows represent radiative transitions and dashed arrows represent non-radiative transitions.

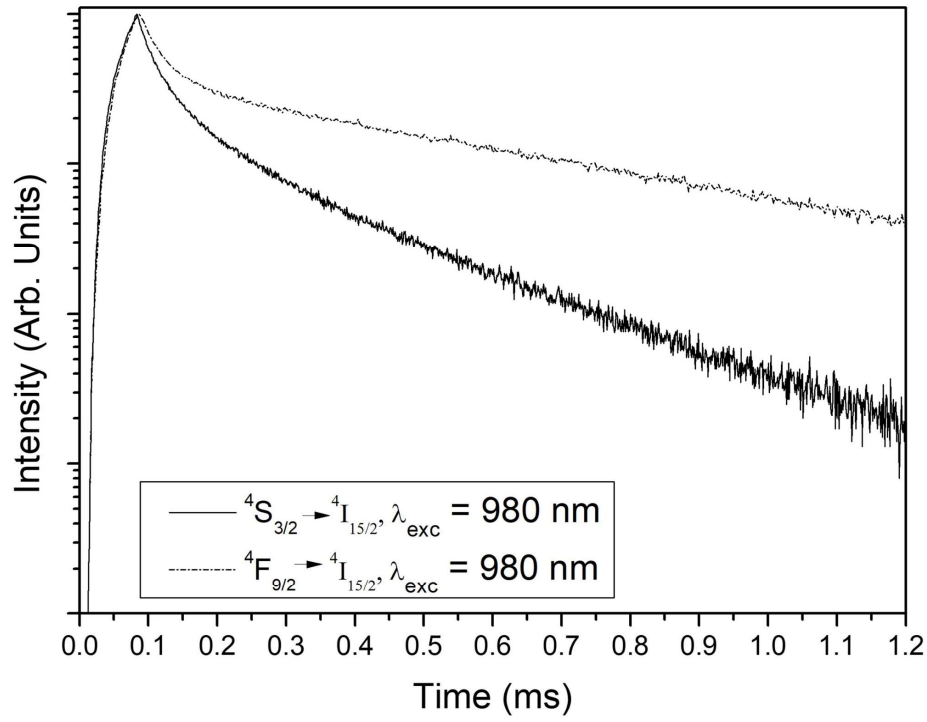


Figure 7. Upconversion fluorescence decay curves for $^4S_{3/2} \rightarrow ^4I_{15/2}$ and $^4F_{9/2} \rightarrow ^4I_{15/2}$ transitions of $\text{La}_{1.90}\text{Er}_{0.10}\text{Ti}_2\text{O}_7$, under excitation at 980 nm.

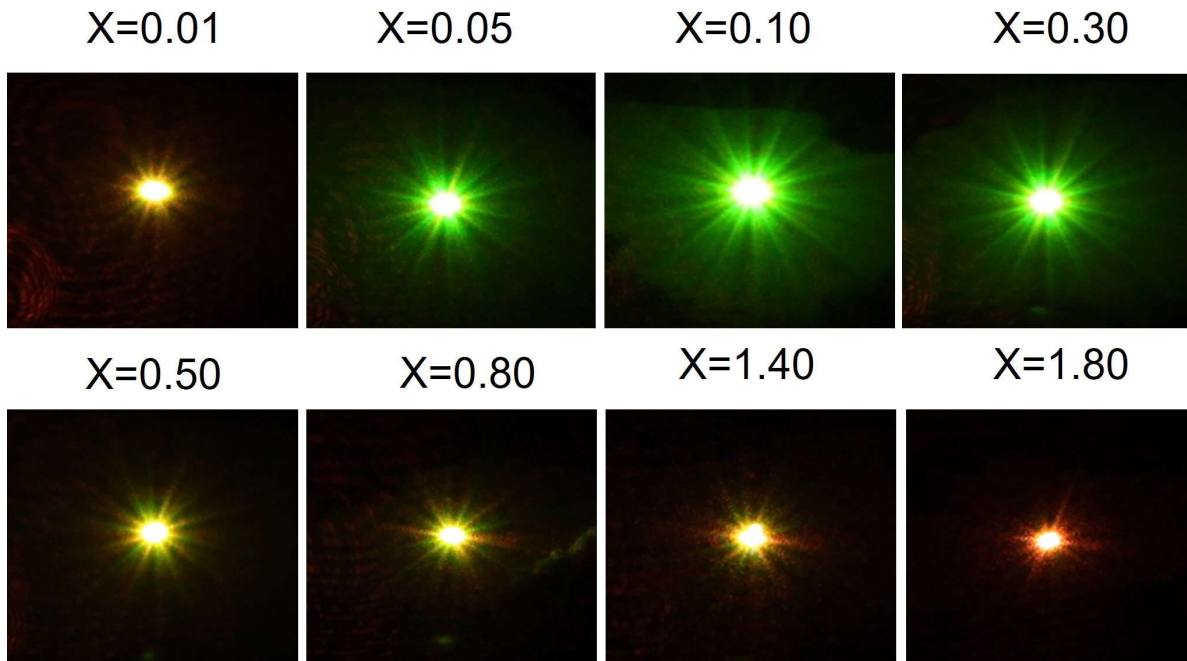


Figure 8. Pictures of $\text{La}_{2-x}\text{Er}_x\text{Ti}_2\text{O}_7$ under laser excitation at 784 nm.

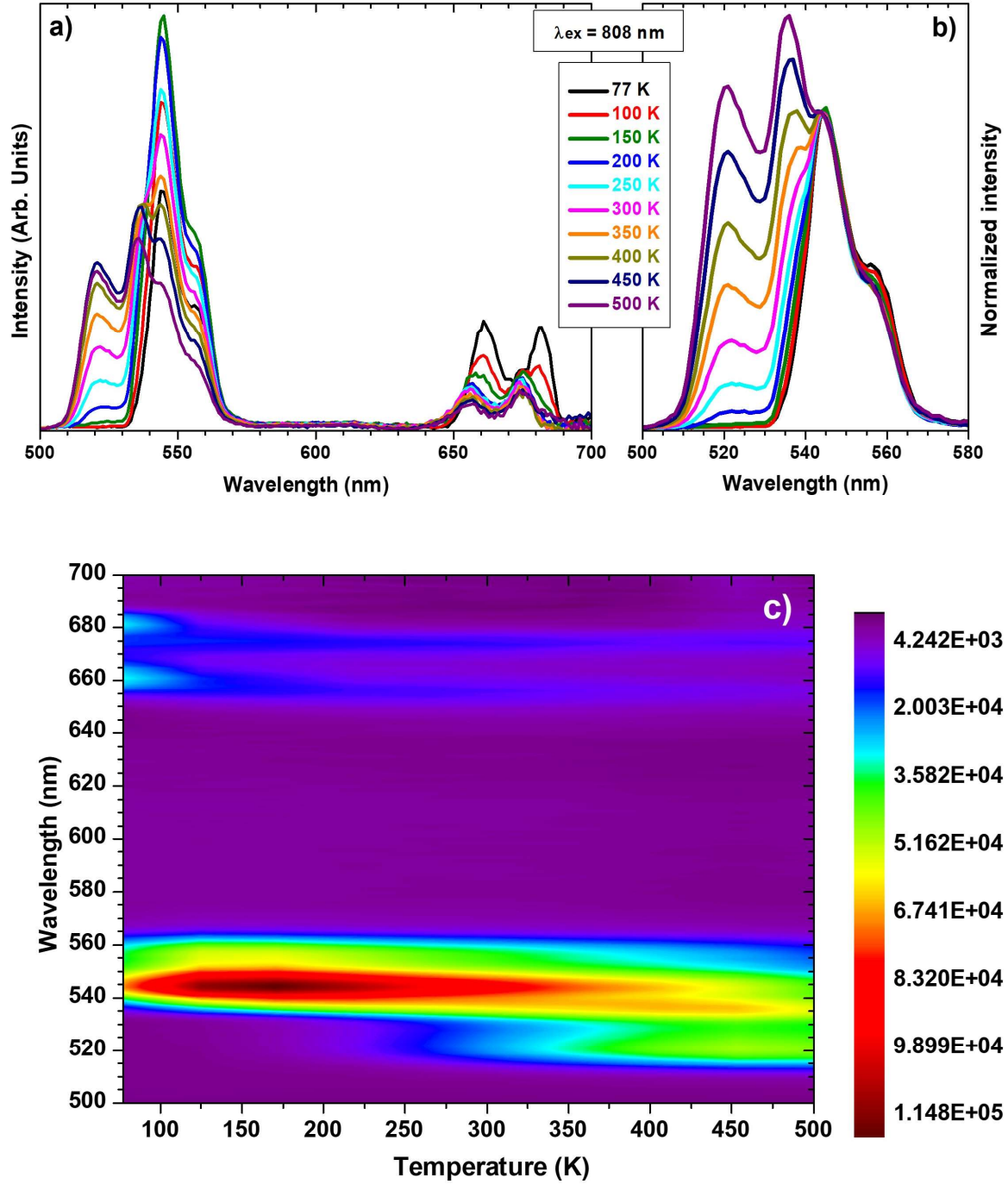


Figure 9. a) Emission spectra of $\text{La}_{1.9}\text{Er}_{0.1}\text{Ti}_2\text{O}_7$ ($\lambda_{\text{ex}} = 808 \text{ nm}$) as function of temperature in a range of 77 to 500 K; b) Normalized (to 544 nm) temperature dependent emission spectra; c) 2D contour map showing the evolution of the emission bands (intensity and position) as a function of the temperature.

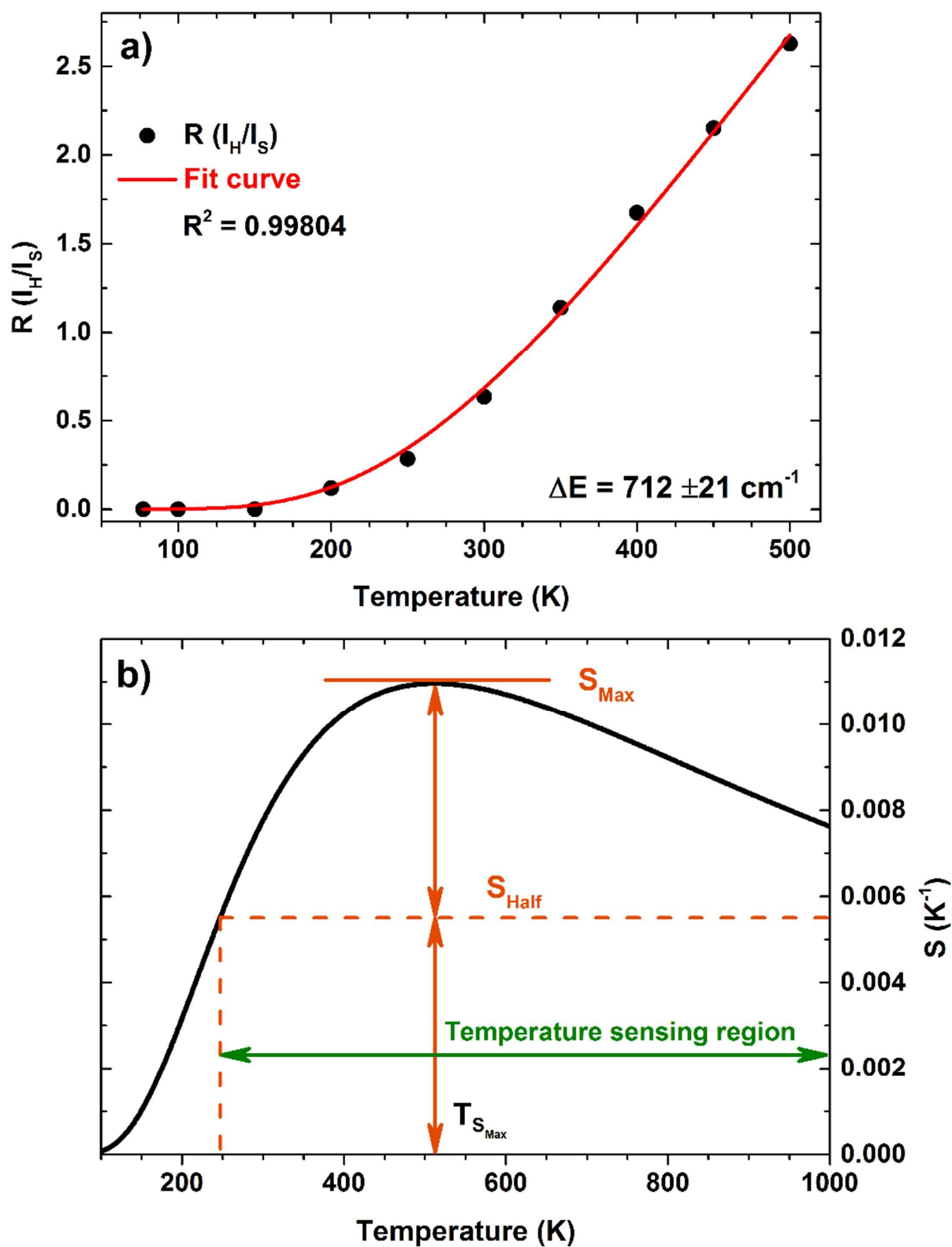


Figure 10. a) Ratio between ${}^2\text{H}_{11/2} \rightarrow {}^4\text{I}_{15/2}$ and ${}^4\text{S}_{3/2} \rightarrow {}^4\text{I}_{15/2}$ transitions as a function of temperature; b) dependence of sensitivity on sample temperature.

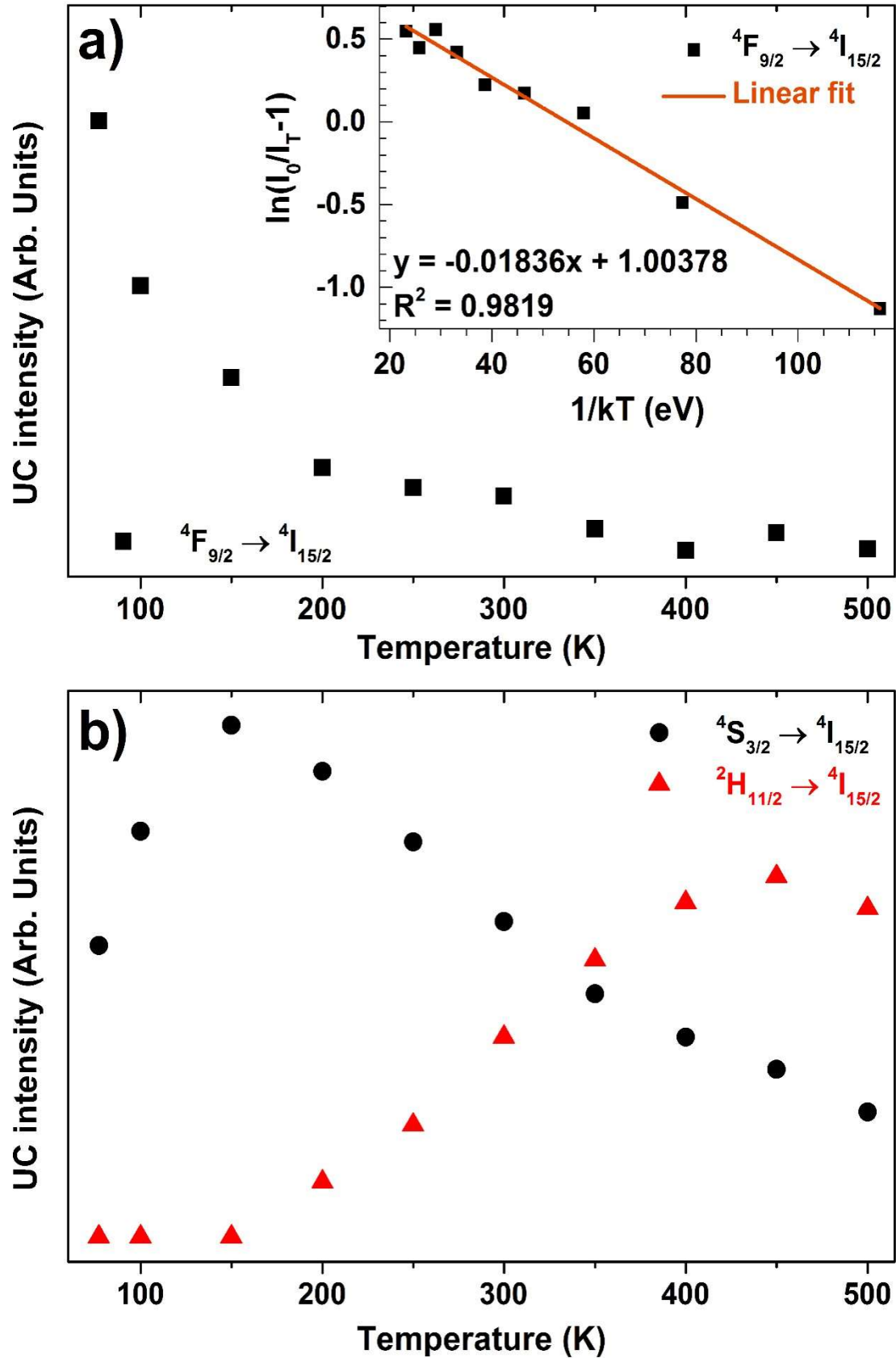


Figure 11. a) Evolution of UC intensity of La_{1.9}Er_{0.1}Ti₂O₇ as a function of the temperature for $^4F_{9/2} \rightarrow ^4I_{15/2}$ transition (inset a plot of $\ln(I_0/I_T - 1)$ vs. $1/T$ for the determination of the activation energy); b) Evolution of UC intensity as a function of the temperature for $^2H_{11/2} \rightarrow ^4I_{15/2}$ and $^4S_{3/2} \rightarrow ^4I_{15/2}$ transitions (curves fitting in red).

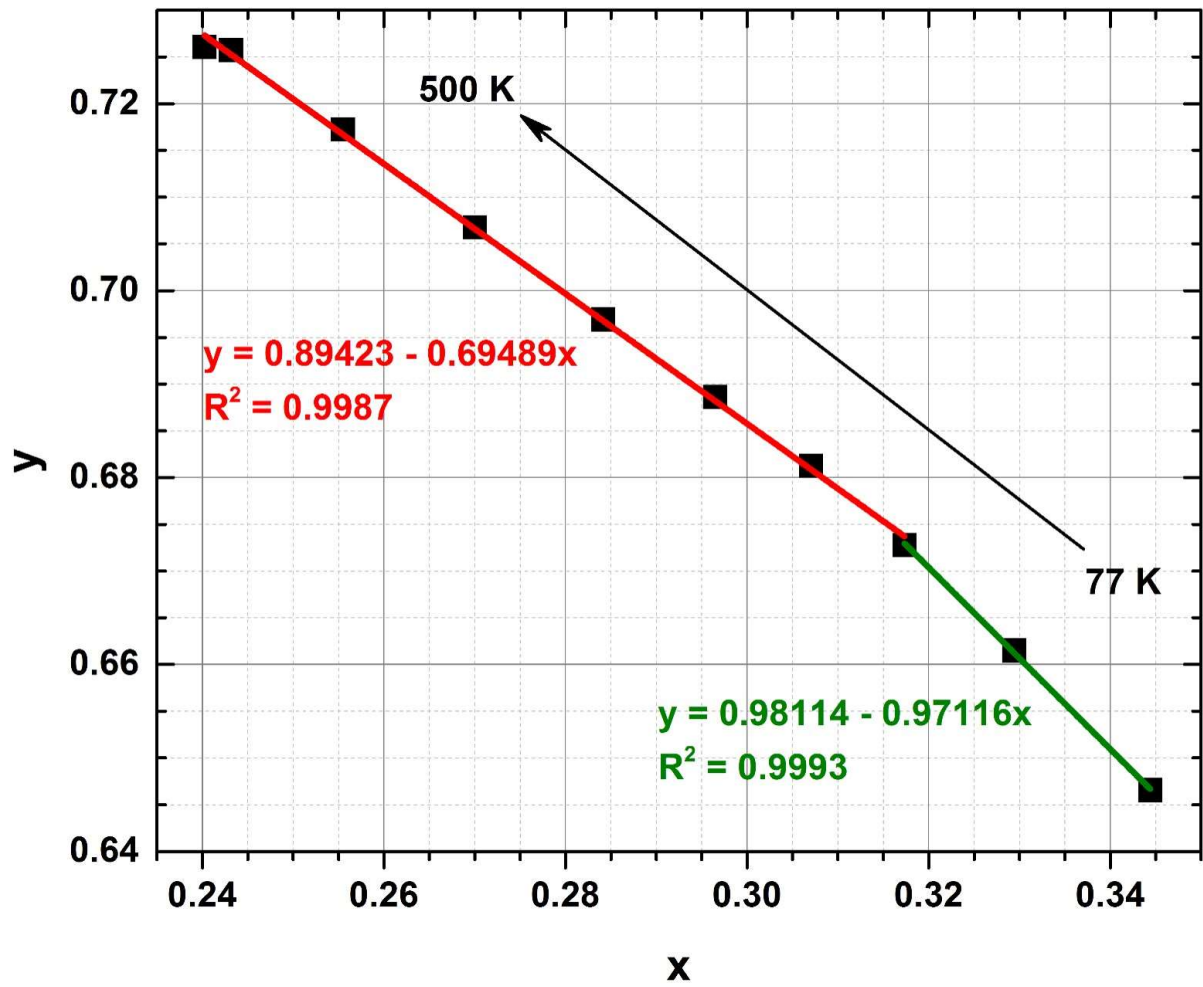


Figure 12. Evolution of the CIE 1931 color coordinates according to the temperature for $\text{La}_{1.9}\text{Er}_{0.1}\text{Ti}_2\text{O}_7$ under 808 nm excitation.

TABLE CAPTIONS

Hosting Matrix	λ_{exc} (nm)	A	ΔE (cm ⁻¹)	S_{max} (K ⁻¹)	T_{max} (K)	T-range (K)	ref
Fluorotellurite glass:Er ³⁺	800	10.25	765	0.0054	540	300- 550	64
Lanthanum Oxysulfide powders: Er ³⁺ /Yb ³⁺	806	8.76	683	0.0109	300	240- 300	65
K ₂ GdF ₅ :Er ³⁺ /Yb ³⁺	980	7.84	690	0.0110	307	307- 570	66
β -NaGdF ₄ :Er ³⁺ /Yb ³⁺	980	7.71	789	0.0037	580	303- 503	67
Silicate glass: Er ³⁺	978	1.87	512	0.0023	-	296- 673	68
CaWO ₄ :Er ³⁺ /Yb ³⁺	980	15.40	755	0.0092	455	294- 923	69
Y ₂ Ti ₂ O ₇ :Er ³⁺ /Yb ³⁺ /Li ⁺	980	8.5	812	0.0067	363	300- 675	70
La _{1.90} Er _{0.10} Ti ₂ O ₇	808	20.73	712	0.0110	512	250- 1373	This work

Table 1. Sensing parameters for several Er³⁺ hosting matrix.